

Massive star formation and tidal structures in HCG 31¹

Ángel R. López-Sánchez

Instituto de Astrofísica de Canarias, E-38200, La Laguna, Tenerife, Spain
angelrls@ll.iac.es

César Esteban

Instituto de Astrofísica de Canarias, E-38200, La Laguna, Tenerife, Spain
cel@ll.iac.es

Mónica Rodríguez

Instituto Nacional de Astrofísica, Óptica y Electrónica, Apdo. Postal 51 y 216, 72000 Puebla, Mexico
mrodri@inaoep.mx

ABSTRACT

We present new broad-band optical and near-infrared CCD imaging together with deep optical intermediate-resolution spectroscopy of the Hickson Compact Group 31. We analyze the morphology and colors of the stellar populations of the galaxies, as well as the kinematics, physical conditions and chemical composition of the ionized gas in order to get a more complete view on the origin and evolution of the system. We estimate the ages of the most recent star formation bursts of the system, finding an excellent consistency among the values obtained with different indicators and starburst models. We find that member F hosts the youngest starburst of the group, showing a substantial population of Wolf-Rayet stars. The chemical abundances are fairly similar in all the members of the group despite their very different absolute magnitudes. We argue that the use of traditional metallicity-luminosity relations based on the absolute B -magnitude is not appropriate for dwarf starburst galaxies, because their luminosity is dominated by the transient contribution of the starburst to the blue luminosity. We think that members E and F of the group are candidate tidal dwarf galaxies because of their high metallicity, their kinematics, and the absence of underlying old stellar populations. Finally, we propose that HCG 31 is suffering several almost simultaneous interaction processes. The most relevant of these processes are: (a) the merging of members A and C, that would have produced two optical tidal tails; and (b) a fly-by encounter between G and the A+C complex, that would have produced an H I tidal tail from the stripping of the external gas of A+C, from which members F and E have originated.

Subject headings: galaxies: starburst — galaxies: interactions — galaxies: abundances — galaxies: kinematics and dynamics — galaxies: clusters: individual: HCG 31

1. Introduction

¹Based on observations made with several telescopes operated on the islands of La Palma and Tenerife by the Isaac Newton Group of Telescopes, Nordic Optical Telescope and Instituto de Astrofísica de Canarias in the Spanish observatories of Roque de Los Muchachos and Teide of the In-

The starburst phenomenon in galaxies was first described by Sargent & Searle (1970), who noted that some galaxies seem to be experiencing strong episodes of star formation. Sargent & Searle estimated that the material available for the produc-

stituto de Astrofísica de Canarias.

tion of stars would be exhausted in a very short time compared to the age of the Universe. Since this discovery, many studies have been performed trying to understand the processes that trigger starburst galaxies. Wolf-Rayet (WR) galaxies are a subset of starburst galaxies that show broad stellar He II λ 4686 emission in their integrated spectra due to WR stars, whose ages are less than 6 Myr. This spectral feature indicates the presence of a substantial population of this sort of massive stars and offers the opportunity to study very young bursts. Making use of population synthesis models it is possible to determine the age of the WR bursts and, consequently, the star formation and its causes can be studied.

In dwarf galaxies, starburst phenomena cannot be understood under the wave-density theory because of their low masses, so other mechanisms are needed. One of the proposed alternative mechanisms for large scale starburst formation is the gas compression by shocks due to the mass lost by galactic winds, followed by the subsequent cooling of the medium. Recent results of this theory (Hirashita 2000) predict an intermittent behavior of the bursts in dwarf galaxies, with long inactivity periods. This theory was first suggested by Thuan (1991). Others authors have proposed galaxy interactions as the massive star formation triggering mechanism (Sanders et al. 1988), although the interactions cannot be with neighbor giant galaxies in most cases (Campos-Aguilar, Moles & Masegosa 1993; Telles & Terlevich 1995). In fact, they seem to be more frequent with low surface brightness galaxies (Taylor, Brinks & Skillman 1993; Taylor et al. 1995, 1996). This led Méndez & Esteban (1999) to suggest that interactions with other dwarf objects could be the main star formation triggering mechanism in dwarf galaxies and, especially in WR galaxies.

Compact groups of galaxies are systems with a high density of galaxies and a low dispersion velocity, constituting the highest density cusps in the non-clustered large-scale structure. They were defined by Hickson (1982) using various richness, compactness and isolation criteria. Hickson et al. (1992) and Barton et al. (1996) extended the compact group definition. The resultant compact group population represents $\sim 1\text{-}2\%$ of the galaxy field and is characterized by aggregates of 4-8 galaxies with mean projected separations of the

order of a component galaxy diameter. The small projected separations and observed signs of interaction imply physical densities as high as those found in the cores of rich clusters of galaxies. In fact, interactions between the group-members are important in some compact groups. Moles et al. (1994) found that star formation rates (SFRs) in galaxies belonging to compact groups are somewhat higher than in field galaxies. Mendez de Oliveira & Hickson (1994) reported morphological interaction signs, like mergers and tidal tails, in many galaxies from Hickson (1982) catalogue of compact groups. Recent studies of interactions in compact groups can be found in Vílchez & Iglesias-Páramo (1998); Iglesias-Páramo & Vílchez (1999, 2001); Verdes-Montenegro et al. (1997, 1998, 2001, 2002); Sulentic et al. (2001); Plana, Amram & Mendez de Oliveira (2002). The finding of the WR characteristics in some of the members of these compact groups allows the study of star formation and its triggering mechanism with detail. Perhaps, one of the best systems to perform this investigation is the WR galaxy NGC 1741 and the compact group where it belongs: HCG 31.

1.1. Brief history of the membership

The compact group HCG 31, at a distance of 54.8 Mpc ($H_0=75 \text{ km s}^{-1} \text{ Mpc}^{-1}$; Vacca & Conti 1992), was identified by Hickson (1982). It is one of the best studied compact groups because of the peculiar morphology of its members that includes tidal tails, a possible merger, irregular structures, and prominent starbursts in its brightest galaxies (see Fig. 1). Hickson (1982) described the group as four galaxies in close proximity, that he called A, B, C and D. He noted that two of them, members A and C, are clearly interacting, and they both actually form NGC 1741 (Mrk 1089, VV524, Arp259). In fact, Mazzarella & Boroson (1993) also classified NGC 1741 as a double nucleus Markarian galaxy. Kunth & Schild (1986) detected the 4686 Å WR feature in the spectrum of the nucleus of galaxy C. This was later confirmed by Rubin, Hunter & Ford (1990). NGC 1741 was included in the first catalogue of WR galaxies by Conti (1991) as one of the most luminous WR galaxies known. Vacca & Conti (1992) obtained the optical spectra of A and C and found that they are dominated by strong nebular emission lines, as expected from the presence of a large number

of hot, massive stars. UV studies performed by Conti, Leitherer & Vacca (1996) revealed that the centre of NGC 1741 is dominated by two main starbursts, which are composed of several intense knots of recent star formation. Johnson et al. (1999) obtained *Hubble Space Telescope* (*HST*) images of the system, dating the main starbursts (A and C) in 5 Myr, and detecting 434 Super Star Clusters (SSCs) in the central knots. Richer et al. (2003) called NGC 1741 the A+C complex, because they considered that A and C are a single kinematical entity.

Member B was classified as a Sm galaxy by Hickson (1982). It shows three different bright knots in H α images (Rubin et al. 1990; Iglesias-Páramo & Vílchez 1997, hereinafter IV97; Johnson & Conti 2000). Its morphology suggests that it is a dwarf spiral or irregular galaxy seen nearly edge-on. Rubin et al. (1990) and Richer et al. (2003) found that it shows solid-body rotation and seems to be kinematically distinct from the A+C complex.

Rubin et al. (1990) identified two nearby additional objects, E and F, and the close galaxy Mrk 1090 (object G), that were all included as new members of HCG 31, as well as the far member Q, that lies 2' to the north of the A+C complex. These authors also determined that D is a background galaxy at a distance of 359 Mpc. IV97 studied the ages of the bursts, and concluded that F is as young as member C. The H I map of the group (Williams, McMahon & van Gorkom 1991) shows that all the galaxies, except D, are embedded in the same neutral cloud. Williams et al. estimated a total hydrogen mass of $2.1 \times 10^{10} M_{\odot}$. Maxima of H I column density are coincident with the galaxies, indicating that they are gas rich.

Hunsberger, Charlton & Zaritsky (1996) proposed several tidal dwarf candidates in HCG 31: one of them corresponds to member F, and the other ones are located at the northeast of the A+C complex. Johnson & Conti (2000) considered E and F as tidal dwarf galaxies, and detected new SSCs in them. Those authors confirmed that F shows a starburst of around 4 Myr, although it can be younger. Iglesias-Páramo & Vílchez (2001) noted 2 tidal objects at the northeast of the A+C complex and 7 tidal objects (including E, F1, F2, and faint H) at the southeast tidal tail, which appears delineated in the H I map. Iglesias-Páramo

& Vílchez (2001) analyzed those objects and concluded that only member F satisfies the escape and self-gravitation conditions to be a tidal dwarf galaxy. Richer et al. (2003) argued that E is an integral part of the A+C complex or is now separating from it. For those authors, the kinematics of member E confirms that the extension of the A+C complex towards E and F is a tidal tail. Richer et al. also suggested that galaxy F could be a tidal fragment of the A+C complex that detached some time ago.

G has a spherical shape in the broad-band images, but IV97 found that it hosts some knots of stellar formation at the northwest. This was confirmed by Johnson & Conti (2000), who found a very asymmetric H α emission, with the star-forming regions forming a U shape along the northwest side. Richer et al. (2003) described G as a small disk galaxy seen nearly face-on because the H α velocity has only a very small gradient across its disk. They also noted that its kinematics is distinct from that of the A+C complex.

1.2. Structure of this paper

In § 2 we present our observations and the data reduction processes. In § 3 we present our optical and near-infrared photometric results, studying the effect of the reddening in the final data. In that section, we also present the results of our intermediate-resolution spectroscopy: physical conditions, chemical abundances, and kinematics of the ionized gas. In § 4 we discuss our results: we analyze the ages of the bursts and the stellar and WR populations, the star formation rates, the luminosity-metallicity relation in the members of HCG 31, the possibility that members E and F are tidal dwarf galaxies, and a revision of the star formation history in HCG 31. We finally present our main conclusions in § 5.

2. Observations and data reduction

2.1. Optical imaging

The images in the *U*, *B*, and *V* filters were taken on 2002 October 23 at the 2.56m Nordic Optical Telescope (NOT) at Roque de los Muchachos Observatory (La Palma, Canary Islands, Spain) during a Spanish Service Night. We used ALFOSC (Andalucía Faint Object Spectrograph and Camera) in image mode with a Loral/Lesser CCD de-

Table 1: Summary of observations

Observations	Telescope	Date	Exp. Time (s)	Spatial ('' pix ⁻¹)	Filter/ grating	P.A. (°)	Spectral (Å pix ⁻¹)	$\Delta\lambda$ (Å)
Broad-band imaging	2.56m NOT	02/10/23	3 × 300	0.176	<i>U</i>
	2.56m NOT	02/10/23	3 × 300	0.176	<i>B</i>
	2.56m NOT	02/10/23	4 × 300	0.176	<i>V</i>
	2.50m INT	03/09/22	2 × 200	0.33	<i>R</i>
	1.55m CST	03/02/04	120 × 20	1.0	<i>J</i>
	1.55m CST	03/02/04	240 × 10	1.0	<i>H</i>
	1.55m CST	03/02/04	360 × 5	1.0	<i>K_S</i>
Intermediate resolution spectroscopy	4.2m WHT	00/12/29	1800 × 4	0.20	R600B	61.0	0.45	3650-5100
	4.2m WHT	00/12/29	1800 × 4	0.36	R136R	61.0	1.49	5300-6650
	4.2m WHT	00/12/30	1800 × 4	0.20	R600B	128.0	0.45	3600-5200
	4.2m WHT	00/12/30	1800 × 4	0.36	R136R	128.0	1.49	5500-6850
	4.2m WHT	00/12/31	1800 × 4	0.20	R600B	133.0	0.45	3660-5050
	4.2m WHT	00/12/31	1800 × 4	0.36	R136R	133.0	1.49	5450-6850

tector (2048×2048 pixels) with a pixel size of $15 \mu\text{m}$ and spatial resolution of $0.188'' \text{ pixel}^{-1}$, and the standard Johnson filters *U*, *B* and *V*. Three or four 300 s exposures were added for each filter to obtain a good signal-to-noise and an appropriate removal of cosmic rays in the final images. The measured full width half maximum (FWHM) of the point-spread function (PSF) was approximately $2.2''$. Images were taken under photometric conditions, and the standard field 98-1119 of Landolt (1992) was used to flux calibrate them. Twilight images of different zones of the sky were taken for each filter in order to perform the flat-field correction. The bias subtraction, flat-fielding and flux calibration of the images were made following standard procedures. All the reduction process was done with IRAF². We obtain the photometry of the integrated flux inside the 3σ contours of each member of HCG 31 over the sky background level.

The image in the *R* (Sloan-Gunn) filter was taken on 2003 September 22 at the 2.50m Isaac Newton Telescope (INT) at Roque de los Muchachos Observatory (La Palma, Canary Islands, Spain). We used the WFC (Wide Field Camera) with a CCD detector (2048×4096 pixels) with a pixel size of $15 \mu\text{m}$ and spatial resolution of $0.33'' \text{ pixel}^{-1}$ at prime focus. Two 200 s exposures were added to remove cosmic-rays. The measured FWHM of PSF was approximately $1.1''$. The standard fields 93-424 and 97-284 of Landolt (1992)

were used to flux calibrate the final image. All the reduction process was done with IRAF following the same procedure explained above.

2.2. Near-Infrared imaging

We used the 1.55m Carlos Sánchez Telescope (CST) at Teide Observatory (Tenerife, Canary Islands, Spain) to obtain the near-infrared images on 2003 February 3. We used the CAIN camera (256×256 pixels) with a pixel size of $40 \mu\text{m}$ and a spatial resolution of $1'' \text{ pixel}^{-1}$ in the wide mode to obtain images in the *J* ($1.2 \mu\text{m}$), *H* ($1.6 \mu\text{m}$) and *K_S* ($2.18 \mu\text{m}$) broad-band filters. We took 20 series of 6 consecutive individual 20 s exposures in *J*, 20 series of 12 individual 10 s exposures in *H* and 30 series of 12 exposures of 5 s duration in *K_S*. Each sequence of exposures was made at slightly different positions to obtain a clean sky image. In this way, we obtained a final image of 20 minutes in *J* and *H*, and a final one of 10 minutes in *K_S*. We repeated this procedure two times for *J* and *H* and three times for *K_S*, and then combined all the images to obtain a single image for each filter. The FWHM PSFs of these final images were $2.4''$, $2.2''$, and $1.9''$ for *J*, *H*, and *K_S*, respectively. Bright and dark dome flat-field exposures were taken for each filter, and were combined to obtain a good flat-field image. The standard stars As13 and As19 (Hunt et al. 1998) were used for the flux calibration.

²IRAF is distributed by NOAO which is operated by AURA Inc., under cooperative agreement with NSF

2.3. Intermediate-resolution spectroscopy

Intermediate-resolution spectroscopy of different galaxies of the group at three slit positions was carried out on 2000 December 29, 30 and 31 with the 4.2m William Herschel Telescope (WHT) at Roque de los Muchachos Observatory (La Palma, Canary Islands, Spain) with the ISIS spectrograph at the Cassegrain focus. Two different CCDs were used at the blue and red arms of the spectrograph: an EEV CCD with a configuration of 4096×2048 pixels of $13 \mu\text{m}$ in the blue arm and a TEK with 1024×1024 of $24 \mu\text{m}$ in the red arm. The dichroic used to separate the blue and red beams was set at 5400 \AA . The slit was $3.7'$ long and $1''$ wide. Two gratings were used, R600B in the blue arm and R316R in the red arm. These gratings give reciprocal dispersions of 33 and 66 \AA mm^{-1} , and effective spectral resolutions of 2.0 and 3.9 \AA for the blue and red arms, respectively. The blue spectra cover from 3600 to 5200 \AA and the red ones from 5400 to 6800 \AA . The spatial resolutions were $0.20'' \text{ pixel}^{-1}$ in the blue and $0.36'' \text{ pixel}^{-1}$ in the red.

Three slit positions of HCG 31 were observed at different position angles, which were chosen in order to cover different members of the group. For each slit position, four 30 minutes exposures were taken and combined to obtain good signal-to-noise and an appropriate removal of cosmic rays in the final blue and red spectra. Comparison lamp exposures of CuAr for the blue arm and CuNe for the red one were taken after each set of spectra. The correction for atmospheric extinction was performed using an average curve for the continuous atmospheric extinction at Roque de los Muchachos Observatory. The observations with slit positions at PA 61° and PA 128° were made at air masses very close to 1. The observations with slit position at PA 133° had air masses between 1.3 and 1.8 but were made very close to the parallactic angle, which varied between 146° and 126° during the observation. Consequently, no correction was made for atmospheric differential refraction.

The absolute flux calibration of the spectra was achieved with observations of the standard stars G191 B2B and Feige 34 (Massey et al. 1988). IRAF software was used to reduce the CCD frames (bias correction, flat-fielding, cosmic-ray rejection, wavelength and flux calibration, sky subtraction) and extract the one-dimensional

spectra for each member of HCG 31. For each two-dimensional spectra several apertures were defined along the spatial direction to extract the final one-dimensional spectra of each galaxy or emission knot. The apertures were centered at the brightest point of each aperture and the width was fixed to obtain a good signal-to-noise spectrum. The internal velocity structure of the knots was not considered because it is analyzed in detail in §3.3.4. All apertures were defined on the "blue" frames. Identical apertures were then used to extract the spectra of the "red" frames. Small two-dimensional distortions were corrected fitting the maxima in the emission of [O II] $\lambda\lambda 3726, 3729$ doublet and H β in the "blue" frames and fitting the continuum emission in the "red" frames.

IRAF software was used to analyze the one-dimensional spectra (see §3.3), but we also used the Starlink DIPSO software (Howarth & Murray 1990) to analyze the profiles of selected bright emission lines as well as those zones where the line profiles were complex, specially the [O II] $\lambda\lambda 3726, 3729$ doublet and the blend of [Ne III] $\lambda 3967$ and H ϵ lines. For each single or multiple Gaussian fit, DIPSO gives the fit parameters (radial velocity centroid, Gaussian sigma, FWHM, etc) and their associated statistical errors.

The journal of all the imaging and spectroscopical observations can be found in Table 1.

3. Results

3.1. Optical imaging

In Figure 1 we show the deep R image of the system. We can distinguish all the component members of HCG 31, from Q that lies $2'$ to the north of the A+C complex to member G to the south. We have labeled all the members of the system, as well as some additional interesting zones that we have also analyzed. The system is dominated by two strong bursts at the center of the A+C complex and a bar that extends to the east, that corresponds to the main body of member A. Two bright zones can be detected in the bar at our spatial resolution. Member A also shows several additional knots delineating a possible tidal tail at the northeast; the zone labeled as A1 is located at the tip of that structure (although Figure 1b shows that the structure or plume extends further to the north). The A+C complex is clearly physi-

cally connected with members B (at the west) and E (at the south) by faint tails or bridges of matter. The extension connecting the A+C complex and member E delineates a clearly defined arc that we call the southwest tail. Apparently, this arc ends at the position of member H or far away towards F. We can appreciate that B consists basically of three main knots that Johnson & Conti (2000) analyzed in $H\alpha$ imaging. Member G also shows a complex morphology with several star-forming regions distributed at its northwest half. Finally, members F1 and F2 can be clearly noted. Their position near a bright star ($m_B=11.9$) has usually been a problem for their photometry, but our new deep images partially solve this problem. We have also marked the position of the faint object H that was detected in our intermediate-resolution spectra. It can also be noted in a previous R band image obtained by Iglesias-Páramo & Vílchez (2001). There are some small non-stellar faint objects surrounding several members of the group, specially to the northeast of the A+C complex and at the south of F1 and F2.

The results of aperture photometry of the optical images for the different members of the group are shown in Table 2. We have also included the values for the knot A1 because this is the zone inside member A for which we have the spectra (see section 3.1). The data are reddening-corrected, as we will discuss below. The area for which we have integrated the flux for each member is irregular and it was defined by the 3σ level isophote in the B image. We have used the same integration area for each object and filter to obtain homogeneous photometric data. Galaxies A and C were measured both together and separately, although it is difficult to define the border area between them. Sky subtraction was performed independently for each member and filter. The photometry for galaxies F1 and F2 is less accurate than for the rest of the objects due to contamination by the bright foreground star. H is not detected in U , B or V , but we have estimated a lower limit to its magnitudes. In any case, we detect H in the R filter (see Fig. 1), with a magnitude of 20.7 ± 0.1 .

We have corrected the observed photometric data for reddening. There are two important contributions to the total extinction by interstellar dust for an extragalactic object: the extinction associated with the dust of the Milky Way in the line

of sight between our Galaxy and the studied object (Galactic extinction) and that due to the dust mixed with the gas of the distant galaxy (extragalactic extinction). From maps of infrared dust emission by Schlegel, Finkbeiner & Davis (1998), we know that the Galactic contribution in the direction of HCG 31 is $E(B - V) = 0.05$, so this fixes a lower limit to the reddening correction. A previous analysis of the extinction toward HCG 31 was presented by IV97, who discussed the results of three papers in which the extinction is analyzed: Rubin et al. (1990) and Mazzarella & Boroson (1993), both using the $H\alpha/H\beta$ ratio, and Williams et al. (1991), who obtain radio H I data. IV97 took these H I-based extinction values as a lower limit to the true ones, since the H I values can only account for the extinction due to dust mixed with the neutral gas in front of the region considered, but not within the H II region. In this way, IV97 assume $E(B - V) = 0.2$ for member B and $E(B - V) = 0.15$ for the rest of the objects in HCG 31.

In our case, we have used the reddening constant, $C(H\beta)$ -obtained from the absorption-corrected intensities of $H\gamma$ and $H\beta$ in our optical spectra of each member- to correct our photometric data. The method used to obtain $C(H\beta)$ from our spectra is described in § 3.3. Finally, we use the relation between $C(H\beta)$ and the extinction in V , A_V , obtained by Kaler & Lutz (1985) and assume the standard ratio of $A_V/E(B - V) = 3.1$. The data in B , U and R were corrected using the Rieke & Lebofsky (1985) extinction correction law for A_B , A_U and A_R respectively. We have adopted the reddening values assumed by IV97 for members D and Q because we do not have spectra for them. For the A+C complex we have assumed the average extinction obtained for A, B and C. The final adopted color excess, $E(B - V)$, for each individual galaxy is shown in Table 2. We have determined the errors for the photometry of each member of HCG 31 considering the FWHM of the PSF, the sky level, and the flux calibration error for each frame.

3.2. Near-Infrared imaging

Near-infrared (hereinafter NIR) photometry of HCG 31 in the JHK bands was presented in the survey of 180 interacting galaxies carried out by Bushouse & Stanford (1992). However, they

Table 2: Results of optical and near-infrared aperture photometry

Knot	$E(B - V)$	m_B	m_J	$U - B$	$B - V$	$V - R$	$V - J$	$J - H$	$H - K_S$
A	0.10	15.31 \pm 0.06	13.96 \pm 0.05	-0.41 \pm 0.12	0.01 \pm 0.12	0.43 \pm 0.11	1.34 \pm 0.12	0.28 \pm 0.10	0.14 \pm 0.12
A1	0.10	17.92 \pm 0.05	16.80 \pm 0.06	-0.58 \pm 0.10	-0.11 \pm 0.10	0.13 \pm 0.11	1.23 \pm 0.12	0.54 \pm 0.12	0.29 \pm 0.14
B	0.18	14.95 \pm 0.04	14.64 \pm 0.05	-0.38 \pm 0.09	0.17 \pm 0.08	0.06 \pm 0.08	0.14 \pm 0.10	0.13 \pm 0.10	0.12 \pm 0.10
C	0.06	14.17 \pm 0.06	14.12 \pm 0.05	-0.66 \pm 0.12	-0.01 \pm 0.12	0.09 \pm 0.11	0.06 \pm 0.12	0.12 \pm 0.10	0.21 \pm 0.12
A+C	0.12 ^a	13.59 \pm 0.04	13.36 \pm 0.05	-0.60 \pm 0.09	0.03 \pm 0.08	0.12 \pm 0.10	0.20 \pm 0.10	0.13 \pm 0.10	0.15 \pm 0.10
D	0.15 ^b	18.47 \pm 0.04	16.60 \pm 0.05	0.36 \pm 0.09	0.68 \pm 0.08	0.47 \pm 0.09	1.19 \pm 0.12	0.27 \pm 0.10	0.53 \pm 0.10
E	0.06	17.90 \pm 0.05	17.64 \pm 0.05	-0.65 \pm 0.10	-0.03 \pm 0.10	0.20 \pm 0.09	0.29 \pm 0.12	0.05 \pm 0.10	0.18 \pm 0.12
F1	0.20	17.81 \pm 0.06	18.05 \pm 0.07	-0.99 \pm 0.12	-0.07 \pm 0.12	-0.04 \pm 0.10	-0.17 \pm 0.14	0.04 \pm 0.17	0.29 \pm 0.30
F2	0.09	19.23 \pm 0.06	19.30 \pm 0.10	-1.01 \pm 0.12	-0.09 \pm 0.12	-0.02 \pm 0.10	0.01 \pm 0.16	0.08 \pm 0.30	0.20 \pm 0.50
G	0.06	14.71 \pm 0.04	14.27 \pm 0.05	-0.43 \pm 0.09	-0.01 \pm 0.08	0.14 \pm 0.08	0.45 \pm 0.10	0.12 \pm 0.10	0.13 \pm 0.10
Q	0.15 ^b	16.51 \pm 0.06	15.83 \pm 0.05	0.07 \pm 0.12	0.11 \pm 0.12	0.24 \pm 0.10	0.77 \pm 0.12
H ^c	0.09	>20.5	>19.5

^aAverage of the value obtained for members A, B, and C.

^bAdopted from IV97.

^c $m_R=20.7\pm0.1$.

only obtained relatively low signal-to-noise data for members A, C, and B, so their photometric values were not very accurate. In Figure 2, we show the logarithmic contour map of HCG 31 in the J filter, and in the B optical filter for comparison purposes. We have not observed member Q in the H and K_S filters. The peculiar morphology of HCG 31 is also recognized in the NIR images. The northeast tail is evident in J , but its brightness is considerably reduced in the H and K_S bands. In fact, it is rather difficult to detect A1 in K_S . The double nucleus and the bar inside the A+C complex appear bright and easily resolved in K_S . The southwest tail is not detected in the NIR images, although member E is clearly detected. In the NIR, the brightest zone of member B is the centre of the galaxy, while its western knot has practically disappeared in K_S . Galaxies F1 and, especially, F2 are difficult to distinguish in H and K_S because of their faintness. The morphology of G in the NIR seems very similar to the optical morphology but the southeast half is brighter in the K_S filter. We have not detected member H but we have estimated a lower limit for its magnitude in each filter.

The results of aperture photometry of the NIR images are also shown in Table 2. The NIR aperture photometry has been performed in the same way as in the case of the optical images. In this case, the shape and size of the apertures were defined by the 3σ level isophote in the J image, and were very similar to the apertures derived for the optical photometry (see the 3σ contours for B and

J filters in Figure 2). We have used the same area for each NIR filter. We have also corrected the observed photometric data for reddening following the same method used for the optical photometry, adopting the Rieke & Lebofsky (1985) extinction corrections for A_J , A_H and A_{K_S} from our calculated A_V value. The NIR photometric errors were calculated following the method explained above for the optical images. The error in $V - J$ color due to the difference in the shape and size between the optical and the NIR images is small when compared with the other uncertainties, but it has also been included.

3.3. Intermediate resolution spectra

Figure 3 shows the three slit positions observed with intermediate-resolution spectroscopy in HCG 31 over our V image. We also indicate the different position angles (PA) observed and the location and size of the regions extracted in order to study the physical conditions and chemical abundances of their ionized gas. The slit at PA 61° covers A1 and members C³ and B; the slit at 128° covers E, H and F, and the one at 133° covers members F and G.

In Figure 4 we show the wavelength and flux calibrated spectra of members C, F1, F2, and G. They show the usual optical emission lines from [O II] $\lambda\lambda 3726, 3729$ to [S II] $\lambda\lambda 6717, 6731$. The

³Following the notation of previous authors, we have called C to the central zone of the A+C complex; it includes the two strong bursts at its center.

[O III] $\lambda\lambda 4959, 5007$ lines are very bright relative to $H\beta$, reflecting the high-excitation of the ionized gas. We can also observe the rather high signal-to-noise ratio of the [O III] $\lambda 4363$ emission line in all these spectra, that will allow us to obtain a good direct determination of the electron temperature. Member C is the most luminous galaxy of HCG 31, and it has the spectrum with the highest signal-to-noise ratio. Members B and G show some underlying stellar absorption in their spectra, which is especially intense in B. Galaxy H is the faintest object detected. It could correspond to one of the SSC found by Johnson & Conti (2000) in the tidal debris of the southwest tail.

The line intensities for each spectrum were measured by integrating all the flux in the line between two given limits and over a fitted local continuum. The observed line intensities must be corrected for interstellar reddening. To do that, we have used the reddening constant, $C(H\beta)$, obtained from the intensities of H I Balmer lines in our optical spectra for each burst. To obtain accurate values of the fluxes of nebular Balmer lines we have also to correct for the underlying stellar absorption. Absorption wings were only evident in $H\alpha$, $H\beta$ and $H\gamma$ in the spectra of members B and G. The underlying stellar absorption is marginal for the rest of the objects. Following Mazzarella & Boroson (1993), we have corrected for absorption making use of the following relation:

$$I_{cor-abs}(\lambda) = I_0(\lambda) \frac{1 + W_{abs}/W_\lambda}{1 + W_{abs}/W_{H\beta}}, \quad (1)$$

where $I_0(\lambda)$ and $I_{cor-abs}(\lambda)$ are the observed and corrected fluxes and W_{abs} , W_λ and $W_{H\beta}$ are the equivalent widths of the underlying stellar absorption of the studied emission line, the equivalent width of the emission line, and the equivalent width of $H\beta$, respectively. The value of W_{abs} can change with the age of the burst, but following Olofsson (1995), we have adopted $W_{abs} = 2 \text{ \AA}$ for all the observed members in HCG 31. This is the same value adopted by Richer et al. (2003). Finally, the spectra were corrected for reddening using the Whitford (1958) law and the value of $C(H\beta)$ derived from the comparison of the $H\beta$, $H\gamma$, and $H\alpha$ relative intensities with the theoretical values expected for case B recombination using Brocklehurst (1971). These theoretical ratios were $I(H\alpha)/I(H\beta)=2.86$ and $I(H\gamma)/I(H\beta)=0.468$,

appropriate for an electron temperature of 10^4 K and electron densities around 100 cm^{-3} . The reddening coefficient $C(H\beta)$, the $H\beta$ line flux, $F(H\beta)$ (corrected by reddening and underlying stellar absorption) and the equivalent width of several lines [$W(H\beta)$ and $W([O III])$] are given in Table 3, while the reddening-corrected line intensity ratios relative to $H\beta$ of each member of HCG 31 are given in Table 4 ($H\alpha$, $H\gamma$ and $H\delta$ intensity ratios are also corrected by underlying stellar absorption). We have estimated the error in the line intensities following the equation given by Castellanos (2000). Colons indicate errors of the order or greater than 40%.

3.3.1. Physical conditions of the ionized gas

Veilleux & Osterbrock (1987) and Dopita et al. (2000) proposed diagnostic diagrams based on emission line ratios useful for classifying the excitation mechanism of an H II region. These diagrams provide an objective spectroscopical separation of H II regions from other classes of narrow line regions associated with active galactic nuclei. We have plotted these two relations in Figure 5 together with our observational data. From the figure, it is evident that our data are consistent with the *loci* of typical H II regions.

As it can be seen in Table 4, we observe the auroral [O III] $\lambda 4363$ emission line in most of the objects: B, C, E, F1, F2, and G. Therefore, we can determine the electron temperature, T_e , using the [O III] ($\lambda 4959 + \lambda 5007$)/ $\lambda 4363$ ratio for those objects. In the case of member C, we also measure the [N II] $\lambda 5755$ line and we can obtain an additional direct determination of T_e for this ion. Electron temperatures are calculated making use of the five-level program for the analysis of emission-line nebulae that is included in IRAF NEBULAR task (Shaw & Dufour 1995). It is usual to use a two-zone approximation to define the temperature structure of the nebulae, assuming $T_e([O III])$ as the representative temperature for high ionization potential ions and $T_e([N II])$ or $T_e([O II])$ for the low ionization potential ones. In our case, we have only determined both temperatures in the case of member C. For the rest of objects, we have assumed the relation between $T_e([O III])$ and $T_e([O II])$ based on the photoionization models by

Table 3: General properties of bursts in HCG 31

	A1	B	C	E	F1	F2	G	H
$-M_B$	15.75 ± 0.06	18.71 ± 0.05	19.43 ± 0.05	15.76 ± 0.06	15.76 ± 0.06	14.34 ± 0.06	18.88 ± 0.05	> 13.1
Slit (")	3.6×1	7.2×1	12.96×1	7.2×1	7.2×1	7.2×1	3.6×1	3.6×1
$C(H\beta)$	0.16 ± 0.06	0.28 ± 0.08	0.09 ± 0.03	0.11 ± 0.05	0.32 ± 0.06	0.14 ± 0.05	0.09 ± 0.05	0.15 ± 0.06
$T_e([O III])$ (K)	8300^a	11500 ± 700	9400 ± 600	11100 ± 1000	12600 ± 1400	12300 ± 1500	11600 ± 700	9000^a
$T_e([O II])^b$ (K)	9900^a	12000 ± 400	10800 ± 300	11800 ± 600	12600 ± 700	12400 ± 800	12000 ± 400	10500^a
$T_e([N II])$ (K)	10800 ± 500
N_e (cm $^{-3}$)	< 100	< 100	210 ± 70	< 100	< 100	< 100	< 100	< 100
Δv_r^c	105 ± 15	132 ± 25	0	-39 ± 15	-66 ± 15	-62 ± 15	-2 ± 15	28 ± 20
$F(H\beta)^d$	2.90 ± 0.23	17.8 ± 0.5	461.3 ± 1.8	15.7 ± 0.6	31.87 ± 0.16	22.76 ± 1.86	25.94 ± 0.59	1.44 ± 0.16
$W(H\beta)$ (Å)	27.0 ± 2.6	12.9 ± 0.5	91.1 ± 2.1	21.1 ± 1.1	218 ± 13	256 ± 43	37.0 ± 1.6	117 ± 30
$W([O III])$ (Å)	46.2 ± 4.4	26.7 ± 1.2	218 ± 4	61.0 ± 1.5	1430 ± 150	1192 ± 135	104 ± 10	347 ± 55

^aCalculated using empirical calibrations of Pilyugin (2001a,b) and Denicoló et al. (2002).

^b $T_e([O II])$ calculated from the relation given by Stasińska (1990).

^cRadial velocity with respect to member C, in km s $^{-1}$.

^dIn units of 10^{-16} erg s $^{-1}$ cm $^{-2}$.

Stasińska (1990):

$$t([O II]) = \frac{2}{t([O III])^{-1} + 0.8}, \quad (2)$$

where $t = T_e/10^4$. It is remarkable that in the case of member C, the direct value of $T_e([N II])$ and the $T_e([O II])$ estimated using (2) coincide (see Table 3). Note that with the alternative linear relation between $T_e([O III])$ and $T_e([O II])$ given by Garnett (1992), the values of $T_e([O II])$ would be around 1000 K lower. In the cases of members A1 and H we do not have direct determinations of the electron temperature. In these cases, the adopted values of T_e are those that reproduce the chemical abundances obtained for these zones applying empirical methods (see § 3.3.2).

All the members of HCG 31 show the $[O II] \lambda\lambda 3726, 3729$ doublet and the $[S II] \lambda\lambda 6716, 6731$ doublet (except members A1 and C, for which S II lines are out of the observed range). We have used both doublets to derive the electron density, N_e , of the ionized gas. Electron densities are always below the low-density limit (< 100 cm $^{-3}$) except for member C, where N_e is slightly higher (210 cm $^{-3}$). The final adopted values of T_e and N_e (or its upper limit) are compiled in Table 3.

3.3.2. Abundance Analysis

Once the electron density and temperature are adopted for each burst, the ionic abundances of He $^+$, O $^+$, O $^{++}$, N $^+$, Ne $^{++}$, S $^+$, S $^{++}$ and Fe $^{++}$ can be derived from our spectra. In the case of O $^+$,

O $^{++}$, N $^+$, Ne $^{++}$, S $^+$, and S $^{++}$ we have used the IRAF NEBULAR task to derive their ionic abundances from the intensity of collisionally excited lines. We have assumed a two-zone scheme for deriving the ionic abundances, adopting $T_e([O III])$ for the high ionization potential ions O $^{++}$, Ne $^{++}$, and S $^{++}$; and $T_e([N II])$ or $T_e([O II])$ for the low ionization potential ions O $^+$, N $^+$, S $^+$ and Fe $^{++}$. These ionic abundances are listed in Table 5. The electron density assumed is 100 cm $^{-3}$ for all the members except C, for which we have used 210 cm $^{-3}$.

An interesting result is the possible detection of C II $\lambda 4267$ in the spectrum of member C (see Figure 6). This is the first time this recombination line is reported in an H II galaxy and opens new possibilities for extragalactic C abundance studies to be done in the future with large aperture telescopes. Although the signal-to-noise ratio of C II $\lambda 4267$ is rather poor, we have calculated the corresponding C $^{++}$ /H $^+$ ratio. We have used the effective recombination coefficients calculated by Davey, Storey & Kisieliu (2000) and $T_e([O III])$ as representative of the zone where this ion is located.

The He $^+$ /H $^+$ ratio has been derived from the brightest He I lines observed in each object using the line emissivities calculated by Smith, Shara & Moffat (1996). We have corrected all the He $^+$ /H $^+$ ratios for the collisional contribution following the calculations by Kingdon & Ferland (1995) and Benjamin, Skillman & Smits (2002). In Table 5

Table 4: Dereddened line intensity ratios with respect to $I(\text{H}\beta)=100$.

Line	f(λ)	A1	B	C	E	F1	F2	G	H
3687 H 19	0.27	0.64:
3692 H 18	0.27	0.85:
3697 H 17	0.27	1.34 \pm 0.29
3704 HeI +H 16	0.26	1.49 \pm 0.30
3712 H 15	0.26	1.39 \pm 0.29
3726 [O II]	0.26	150 \pm 25	189 \pm 18	109.1 \pm 3.8	131 \pm 11	64.5 \pm 4.3	84 \pm 12	171 \pm 11	214 \pm 46
3729 [O II]	0.26	214 \pm 33	281 \pm 24	123.1 \pm 4.1	217 \pm 17	96.7 \pm 5.6	126 \pm 16	240 \pm 15	295 \pm 56
3734 H 13	0.26	2.13 \pm 0.25
3750 H 12	0.26	2.36 \pm 0.27	...	3.4:	4.2:
3771 H 11	0.26	2.92 \pm 0.28	...	4.0:	4.9:	0.33:	...
3798 H 10	0.26	...	5.8:	4.40 \pm 0.40	...	4.6:	6.9:	0.88:	...
3819 He I	0.25	0.50:
3835 H 9	0.24	...	7.1:	6.13 \pm 0.53	...	7.2 \pm 3.5	8.2:	2.6:	...
3869 [Ne III]	0.23	17.6:	31.8 \pm 6.5	15.09 \pm 0.87	35.1 \pm 9.3	39.4 \pm 9.7	32 \pm 11	28.6 \pm 3.7	26.1:
3889 He I	0.22	13.7:	17.5 \pm 6.1	16.73 \pm 0.92	16.6 \pm 6.6	21.0 \pm 6.0	21.8 \pm 9.5	14.7 \pm 2.2	...
3968 [Ne III]	0.21	...	3.9 \pm 1.1	5.11 \pm 0.81	5.2 \pm 1.8	10.3 \pm 1.2	8.4 \pm 1.7	5.9 \pm 1.5	12.3:
3970 He	0.21	13.8:	13.2 \pm 1.9	4.49 \pm 0.74	7.8 \pm 1.5	14.5 \pm 1.3	13.3 \pm 2.2	12.4 \pm 1.9:	...
4026 He I	0.20	1.14 \pm 0.20	...	1.8:
4068 [S II]	0.19	1.85 \pm 0.21	6.4:	3.1 \pm 1.7	...	3.2:	...
4076 [S II]	0.19	0.54 \pm 0.16
4101 H δ^a	0.18	23 \pm 11	23.8 \pm 2.5	23.2 \pm 0.8	25.3 \pm 6.0	25.0 \pm 4.5	24.7 \pm 8.3	21.2 \pm 2.1	19.4:
4244 [Fe II]	0.15	0.40:
4266 C II	0.15	0.22:
4287 [Fe II]	0.14	...	2.5:	0.78 \pm 0.12
4340 H γ^a	0.135	47 \pm 15	46.9 \pm 5.5	46.9 \pm 1.0	46.9 \pm 5.5	46.9 \pm 4.6	46.9 \pm 9.5	46.9 \pm 2.3	47 \pm 23
4359 [Fe II]	0.13	0.53 \pm 0.12
4363 [O III]	0.13	2.8:	2.4 \pm 1.3	1.22 \pm 0.12	2.44 \pm 0.94	6.96 \pm 0.66	4.9 \pm 1.3	3.1 \pm 1.8	...
4471 He I	0.10	5.9:	3.6:	3.82 \pm 0.24	...	4.8 \pm 1.7	4.5:	6.0:	...
4658 [Fe III]	0.05	...	2.5:	1.23 \pm 0.13	4.1:	2.0:	...
4713 He I	0.05	0.44 \pm 0.10
4861 H β	0.00	100 \pm 16	100 \pm 5	100 \pm 1	100 \pm 5	100 \pm 2	100 \pm 16	100 \pm 5	100 \pm 35
4881 [Fe III]	0.00	0.35 \pm 0.10	2.3:	0.42:	...
4922 He I	-0.01	0.75 \pm 0.09	3.1:	...	1.8:	1.4:	...
4959 [O III]	-0.02	64 \pm 15	80.3 \pm 4.5	77.5 \pm 0.7	90 \pm 12	184 \pm 12	137 \pm 25	103 \pm 3	52.2:
4986 [Fe III]	-0.02	...	7.3 \pm 1.7	1.39 \pm 0.15	4.9:	1.9:	...	1.6:	...
5007 [O III]	-0.03	197 \pm 32	243 \pm 10	232 \pm 2	274 \pm 38	546 \pm 23	413 \pm 47	306 \pm 7	136 \pm 28
5016 He I	-0.03	...	4.8:	2.22 \pm 0.19	...	1.7:	2.7:	2.3:	...
5161 [Fe II]	-0.04	0.43:
5200 [N I]	-0.05	1.34 \pm 0.21
5518 [Cl III]	-0.17	0.30:
5538 [Cl III]	-0.18	0.33:	1.8:	...
5755 [N II]	-0.21	0.49 \pm 0.05
5876 HeI	-0.23	14.2 \pm 2.5	13.6 \pm 1.5	11.2 \pm 0.4	9.46 \pm 0.82	11.0 \pm 2.6	11.0 \pm 1.1	12.0 \pm 0.9	13.8:
5980 Si II	-0.25	0.21:
6300 [O I]	-0.30	21.0 \pm 2.7	12.0 \pm 0.6	3.53 \pm 0.10	8.19 \pm 0.45	3.9 \pm 1.1	5.5 \pm 1.9	7.86 \pm 0.60	15.4:
6312 [S III]	-0.30	...	0.67:	0.86 \pm 0.03	1.3:	1.8:	1.5:	2.2:	...
6347 Si II	-0.31	0.18:
6364 [O I]	-0.31	2.1:	4.9:	1.12 \pm 0.03	2.6:	1.3:	1.1:
6371 Si II	-0.31	0.22:
6548 [N II]	-0.34	17.0 \pm 1.8	8.54 \pm 0.85	10.9 \pm 0.1	10.6 \pm 0.3	4.54 \pm 0.31	3.91 \pm 0.45	9.2 \pm 1.5	18.5:
6563 H α^a	-0.34	286 \pm 9	286 \pm 2	286 \pm 1	286 \pm 2	286 \pm 3	286 \pm 6	286 \pm 3	286 \pm 76
6584 [N II]	-0.34	36.0 \pm 2.4	28.9 \pm 0.9	29.7 \pm 0.2	25.6 \pm 0.7	9.82 \pm 0.38	10.2 \pm 0.7	30.2 \pm 1.7	30 \pm 14
6678 He I	-0.35	...	3.0:	3.12 \pm 0.03	2.38 \pm 0.37	3.33 \pm 0.17	3.39 \pm 0.38
6716 [S II]	-0.36	...	14.1 \pm 0.3	...	42.2 \pm 0.3	17.1 \pm 0.3	19.2 \pm 0.4	47.4 \pm 0.6	56 \pm 5
6731 [S II]	-0.36	...	10.1 \pm 0.3	...	29.6 \pm 0.4	11.8 \pm 0.2	14.0 \pm 0.4	33.4 \pm 0.6	40 \pm 4

^aCorrected by underlying stellar absorption assuming $W_{abs}=2 \text{ \AA}$.

we present the He^+/H^+ ratios for each individual He I line and the final adopted average value for each object $\langle \text{He}^+/\text{H}^+ \rangle$.

Although we detect the [Fe II] $\lambda 4244$, $\lambda 4287$, and $\lambda 5161$ emission lines in member C, the Fe^+ abundance cannot be calculated because these lines are affected by fluorescence (Verner et al. 2000). The Fe^{++} abundances have been derived using a 34 level model atom that uses the collision strengths calculated by Zhang (1996) and the transition probabilities given by Quinet (1996). We have used the intensity ratio of the [Fe III] $\lambda \lambda 4658, 4986$ lines to derive a further estimate of N_e in member C (the only region where the intensities measured for these lines have low uncertainties). We find $N_e = 140 \pm 50 \text{ cm}^{-3}$, in agreement with the value obtained from the [O II] diagnostic lines.

The total abundances have been determined for O, N, S, and Fe. The absence or weakness of the He II $\lambda 4686$ line implies a negligible amount of O^{3+} in the nebula. Therefore, we can adopt the usual relation $\text{O}/\text{H} = \text{O}^+/\text{H}^+ + \text{O}^{++}/\text{H}^+$. For N, we have assumed the standard ionization correction factor by Peimbert & Costero (1969): $\text{N}/\text{O} = \text{N}^+/\text{O}^+$, which is a reasonably good approximation for an object with the excitation degree of the objects of HCG 31. We have measured two ionization stages of S in five of the objects. Taking into account the relatively large ionization degree of the spectra, some contribution of S^{3+} is expected. This ion does not show emission lines in the optical region. Therefore, a lower limit to the S abundance is given. For Fe, the total abundances have been obtained from the relation (Rodríguez & Rubin 2003):

$$\left[\frac{\text{Fe}}{\text{H}} \right] = \left[\frac{\text{O}^+}{\text{O}^{++}} \right]^{0.09} \left[\frac{\text{Fe}^{++}}{\text{O}^+} \right] \left[\frac{\text{O}}{\text{H}} \right]. \quad (3)$$

The two objects with the best Fe/H determinations in HCG 31 show $\log(\text{Fe}/\text{O}) = -1.87$ (member B) and $\log(\text{Fe}/\text{O}) = -2.12$ (member C). In a recent paper, Rodríguez (2003) has determined the Fe/O ratios in two giant H II regions of the Local Group with O abundances similar to those of our galaxies: 30 Dor in the LMC ($\log(\text{Fe}/\text{O}) \simeq -2.3$) and N88A in the SMC ($\log(\text{Fe}/\text{O}) \simeq -1.6$). The Fe/O ratios of these giant H II regions (located in dwarf irregular star-forming galaxies) are similar to the values we obtain for the galaxies of

HCG 31. These values are much lower than the solar abundance: $\log(\text{Fe}/\text{O}) = -1.29$ (Holweger 2001). The true Fe/O ratio in a given object depends on two factors: the intrinsic value of Fe/O (in gas and dust), which depends on the star formation history of the system, and the amount of Fe depleted in dust grains. Assuming a solar value for the intrinsic Fe/O in our galaxies, we estimate that $\sim 80\%$ of the Fe atoms are depleted onto dust grains.

For those objects without direct determination of T_e (objects A1 and H) we have derived the total O abundance making use of empirical calibrations. We have used the R_{23} parameter:

$$R_{23} \equiv \frac{I([\text{O II}] 3727) + I([\text{O III}] 4959 + 5007)}{I(\text{H}\beta)}, \quad (4)$$

and the excitation parameter, P :

$$P \equiv \frac{I([\text{O III}] 4959 + 5007)}{I(\text{H}\beta)} \frac{1}{R_{23}}, \quad (5)$$

(Pilyugin 2001a,b) and the [N II] $\lambda 6584/\text{H}\alpha$ ratio (Denicoló, Terlevich & Terlevich 2002). In Table 5 we also include the values obtained with the empirical calibrations for all the members. The objects in HCG 31 have O abundances that do not permit to discern between the high metallicity branch (calibrated by Pilyugin 2001a) or the low metallicity branch (calibrated by Pilyugin 2001b). We have adopted the average value between both calibrations; this seems not to be a bad choice because these values are rather similar (to within 0.1 dex) to the ones obtained from direct determination of T_e . In the other hand, the abundances obtained from the empirical calibrations of Denicoló et al. (2002) are about 0.2 to 0.3 dex higher than those derived from direct methods, except for members F1 and F2 (the lowest metallicity objects). Finally, we have assumed that the O/H abundance ratios of A1 and H are the average value between the three mentioned empirical calibrations. Nevertheless, the true O/H abundance ratios of A1 and H could be somewhat lower than the values indicated in Table 5.

The O/H ratios obtained from direct determination of the electron temperatures (all the objects except A1 and H), are rather similar and range between 8.0 and 8.2 (in units of $12 + \log(\text{O}/\text{H})$). There are several previous determinations

Table 5: Chemical abundances of bursts in HCG 31

	A1	B	C	E	F1	F2	G	H
12+log O ⁺ /H ⁺	8.15 ^a	7.93±0.09	7.82±0.07	7.83±0.13	7.39±0.11	7.53±0.17	7.76±0.09	8.20 ^a
12+log O ⁺⁺ /H ⁺	8.15 ^a	7.73±0.08	8.00±0.04	7.83±0.07	7.96±0.06	7.87±0.08	7.82±0.06	7.87 ^a
12+log O/H	8.35 ^b	8.14±0.09	8.22±0.05	8.13±0.10	8.07±0.07	8.03±0.11	8.15±0.08	8.37 ^b
12+log O/H ^c	8.22	8.22	8.15	8.18	8.12	8.13	8.18	8.33
12+log O/H ^d	8.47	8.39	8.40	8.36	8.06	8.02	8.41	8.41
−log(N/O)	1.21:	1.39±0.14	1.12±0.10	1.26±0.19	1.27±0.19	1.43±0.28	1.31±0.13	1.33:
12+log N/H	7.24:	6.74±0.23	7.10±0.15	6.87±0.29	6.79±0.26	6.61±0.37	6.83±0.20	7.04:
log C ⁺⁺ /O ⁺⁺	+0.32:
12+log Ne ⁺⁺ /H ⁺	7.06:	7.31±0.19	7.29±0.17	7.41±0.27	7.16±0.25	7.11±0.31	7.26±0.15	7.66:
12+log S ⁺ /H ⁺	...	5.57±0.06	5.67±0.08 ^e	6.06±0.10	5.60±0.06	5.67±0.09	6.09±0.05	6.30
12+log S ⁺⁺ /H ⁺	...	5.97:	6.44±0.09	6.31:	6.25:	6.21:	6.17:	...
12+log S/H	...	>6.16	>6.55	>6.55	>6.38	>6.36	>6.48	...
12+log He ⁺ /H ⁺ (4471)	11.08:	10.87:	10.88±0.04	...	10.99±0.22	10.96:	11.09:	...
12+log He ⁺ /H ⁺ (5876)	11.01:	11.01±0.10	10.90±0.03	10.85±0.11	10.92±0.20	10.92±0.16	10.95±0.08	11.01:
12+log He ⁺ /H ⁺ (6678)	...	10.90:	10.91±0.03	10.80±0.14	10.95±0.12	10.96±0.15
< 12 + log He ⁺ /H ⁺ >	11.01:	11.01±0.10	10.90±0.03	10.83±0.13	10.96±0.18	10.94±0.16	10.95±0.08	11.01:
12+log Fe ⁺⁺ /H ⁺	...	6.04±0.14	5.71±0.09	6.06:	5.54:	...	5.75:	...
12+log Fe/H	...	6.27±0.23	6.10±0.16	6.36:	6.16:	...	6.14:	...
Z/Z _⊙ ^f	0.46	0.28±0.07	0.34±0.04	0.28±0.07	0.24±0.04	0.22±0.06	0.29±0.06	0.48

^aCalculated using T_e estimated from empirical calibrations.

^bAverage of values obtained using the empirical calibrations of Pilyugin (2001a,b) and Denicoló et al. (2002).

^cAverage of values obtained using the R₂₃ and P parameters and the empirical calibration of Pilyugin (2001a,b).

^dDetermined using the [N II]/H α ratio (Denicoló et al. 2002).

^eDetermined from the [S II] $\lambda\lambda 4068, 4076$ emission lines.

^fAssuming $Z_{\odot} = 8.69 \pm 0.05$ (Allende Prieto, Lambert & Asplund 2001).

of the chemical abundances for some of the members of the group. For member A, we have values of 8.30 (Rubin et al. 1990), 8.04 ± 0.06 (Izotov & Thuan 1998), and 8.1 ± 0.2 (Richer et al. 2003). These determinations are based on temperatures obtained from the measurement of the [O III] $\lambda 4363$ line, and are lower than the value of O/H = 8.35 we obtain for A1 from empirical calibrations. Therefore, and taking into account the systematically higher abundances given by the empirical calibrations, we will adopt the value by Izotov & Thuan (1998) as representative of member A. We prefer the determination of these authors because of the high quality of their spectrum. In the case of the brightest object, member C, our value of 8.22 ± 0.05 is consistent with previous determinations by Rubin et al. (1990), Vacca & Conti (1992) and Richer et al. (2003). Richer et al. (2003) obtain a direct determination of T_e for F1 (with a rather poor measurement of the [O III] $\lambda 4363$ line) and determine O/H = 8.1 ± 0.2 , which is very similar to our value of 8.07 ± 0.07 . Finally, we obtain the first direct O abundance determinations for members B, E, F2, and G. The O/H ratios implied by Garnett (1992) linear relation be-

tween T_e ([O III]) and T_e ([O II]) would be slightly higher, by 0.01 dex (members F1 and F2) and 0.10 dex (member C). The variation is almost negligible in the case of N/H. These variations do not affect qualitatively to our conclusions.

In the case of C, we have only an uncertain determination of C⁺⁺/H⁺ for member C. Following Esteban et al. (2002) and the photoionization models of Stasińska (1990) and Garnett et al. (1999), we can assume C⁺⁺/O⁺⁺ = C/O as representative for this object. We obtain log(C⁺⁺/O⁺⁺) = +0.32:, which is an extremely high value. Values so high have never been reported for any extragalactic object (see the compilation of Garnett 2003). There are several determinations of the C⁺⁺/O⁺⁺ ratio obtained from the C II λ 4267 line for giant H II regions of the Local Group. Esteban et al. (2002) have obtained values of log(C⁺⁺/O⁺⁺) = −0.19 and −0.39 for NGC 604 and NGC 5461, respectively, and Peimbert (2003) derived −0.50 for 30 Dor. These values correspond to the ratio of ionic abundances determined from C II and O II recombination lines, which give systematically larger abundances relative to H than the collisionally

excited lines. For these three reference objects: NGC 604, NGC 5461, and 30 Dor, we can calculate the C^{++}/O^{++} ratio obtained from the C II $\lambda 4267$ and the [O III] lines (the valid quantity to compare with the ratio we obtain for member C) and we get larger ratios ($\log(C^{++}/O^{++})=+0.01$ dex at most), but never as high as the ratio we obtain for member C. A possible explanation is that we have simply overestimated the intensity of the weak C II $\lambda 4267$ line by a factor of 2, but there are three other possible explanations:

1. the C II $\lambda 4267$ line has been misidentified. This is quite unlikely, because its wavelength coincides exactly with the expected one for that line. There is not any other observable nebular line (or stellar emission feature) at or very near ($\pm 1\text{\AA}$) that wavelength, its width is similar to that of the other nebular lines of that spectral zone;
2. the line is abnormally intense due to an unknown exotic radiative process;
3. the difference between abundances derived from collisionally excited and recombination lines of the same ion is especially large for this object (see Esteban 2002 for a review on this problem in H II regions).

If the last reason is the real one, it could be related to the presence of very strong temperature fluctuations in the ionized gas of member C. This fluctuations would be stronger than in any other known H II region to account for the extremely large value of the C^{++}/O^{++} ratio and would imply that the true metallicity of the object should be much larger, and closer to the solar value.

3.3.3. The Wolf-Rayet bump

The blue WR bump between 4650 and 4698 \AA can be clearly observed in member C (see Fig. 7). It is a blend of emission features of He (He II $\lambda 4686$), C (C III/C IV $\lambda 4650$), and N (N III $\lambda 4640$) of WR stars. The strength of these lines can be used to estimate the number of WR stars in a galaxy (e.g. Vacca & Conti 1992, Schaerer & Vacca 1998). In the spectrum of member C, the strongest contribution is He II $\lambda 4686$, although there is a nearby relatively bright [Fe III] line. Kunth & Schild (1986) reported the first He II

$\lambda 4686$ line in the spectrum of the main body of HCG 31, but they also noted the N III $\lambda 4640$ feature. Guseva, Izotov & Thuan (2000) detected N III $\lambda 4512\lambda$ and Si III $\lambda 4565$ emission lines, as well as the N II $\lambda 5720-40$ one. Despite a possible contribution of nebular emission, these features are related to WN stars, although N II $\lambda 5720-40$ could be contaminated by other WR subtypes. The observed differences between our spectrum of member C and the previously reported ones could be due because we are not observing the same region inside the A+C complex. Guseva et al. (2000) remarked that the WR population in the main body of HCG 31 is dominated by WNL stars, because the C IV $\lambda 5808$ \AA emission feature (the red WR bump) was not detected in their spectrum. We also do not detect that spectral feature in any of our spectra.

We have detected a faint nebular He II $\lambda 4686$ emission line in member F1 that has not been previously reported. This feature seems also to be present in F2. Moreover, a very faint blue WR bump seems to be present in the spectra of A1 and B.

3.3.4. Kinematics of HCG 31

We have determined the mean radial velocity of each member of HCG 31 from the centroid of $H\beta$ and [O III] $\lambda 5007$ emission lines in the brightest zone of each galaxy. We have taken the most luminous member, C, as reference for the radial velocities of the group; its heliocentric velocity is 4042 km s^{-1} . The relative radial velocities of the group members are given in Table 3. They span a narrow interval of values with a maximum difference of about 200 km s^{-1} . Our velocities are in very good agreement with those obtained by Rubin et al. (1990) and Richer et al. (2003) from their optical spectra and those obtained by Williams et al. (1991) from their H I velocity map. We find that members E, F1, F2, and G, all of them located to the southern part of the system, show negative values of the velocity. This is consistent with the general trend observed in the H I velocity map of Williams et al. (1991). However, the new object H has a somewhat abnormal positive velocity relative to its position. The other northern members of the group, A1 and B, show positive velocities.

We have also studied the kinematics of the ion-

ized gas via the spatially resolved analysis of bright emission line profiles along each slit position. We have extracted zones of 5 pixels ($1''$ in the spatial direction) covering all the extension of the line emission in the three slit positions shown in Figure 3. This analysis has been performed via Gaussian fitting making use of the Starlink DIPSO software. For each zone, we have analyzed the profiles of $H\beta$ and the $[O\ III]\ \lambda\lambda 4959, 5007$ lines (the brightest lines of the spectra taken with the blue arm of the spectrograph, with the highest spectral resolution) using one, two or all of these lines depending on the signal-to-noise of each spectrum. The final adopted values are the average of the results for all the individual lines used in the analysis of each individual zone. In all the cases, the line emission profiles were well fitted by a single Gaussian fit and therefore no complex profiles were needed. In Figure 8 we show the position-velocity diagrams for the three slit positions. All the velocities are referred to the mean heliocentric velocity of member C (4042 km s^{-1}). The position of the different galaxy members of the group is also indicated on Figure 8. Rubin et al. (1990) also show position-velocity diagrams for A, B, C, and E (extracted every $3.5''$ along the slit) and are very similar to ours in the zones in common. Richer et al. (2003) obtain Fabry-Perot observations of the group in $H\alpha$ and also present position-velocity diagrams for A, B, and C at the same positions, angles, and spatial resolution as Rubin et al. (1990).

Our position-velocity diagram for C, as well as that obtained by Rubin et al. (1990), shows a sinusoidal pattern in the center of the object. It is evident that the velocity reverses in the central region with counter motions of the order of 50 km s^{-1} . This is a traditional diagnostic of interaction and merging of galaxies (e.g. Schweizer 1982; Rubin et al. 1990) and indicates that a merging process is ongoing in the central zone of the A+C complex. However, Richer et al. (2003) find that members A and C seem to be a single kinematical entity in their Fabry-Perot data. Perhaps, Richer et al. do not observe this feature due to the lower sensitivity and lower spatial resolution of their position-velocity diagrams.

In the case of member B, our results are consistent with those from other authors. Its variation of velocity across the slit is rather linear indicating that the galaxy is basically rotating as a

solid-body, although some slight deviations from that (just concentrated in the nucleus) are present. There is a very faint nebular emission between galaxies A and B for which it was not possible to carry out the profile analysis. However, the adjacent external zones of both galaxies seem to indicate a continuous linear connection in velocity of the ionized gas between both objects. The solid-body rotation pattern of member B could be affected by a possible tidal streaming motion between B and the A+C complex, at least in the external zones. As in the case of member B, the ionized gas between zone A1 and the northeast extension of member C seem to follow a smooth linear increase of radial velocity.

The position-velocity diagrams for PA 133° and PA 128° are rather complex. The slit position at PA 133° (Fig. 8b) was intended to cover precisely the major axis of F1 and F2, and crosses the northern diffuse outskirts of member E and the center of member G. The slit position at PA 128° (Fig. 8c) covers the main body of E, the zone around H, and the north of F1 and F2. In Figure 8b it can be seen that the diffuse faint area at the north of member E (indicated as “E”) shows a linear variation with a quite wide amplitude of about 70 km s^{-1} . This behavior is quite different to that shown by the main body of object E (Fig. 8c), which, interestingly, does not show traces of the linear behavior of the diffuse gas at the north. In fact, the central part of E shows a narrow sinusoidal behavior with a velocity amplitude of about $30\text{--}40\text{ km s}^{-1}$. This suggests that perhaps we are seeing two different kinematical objects that coexist in apparent close proximity. As it can be seen in the *R*-band image shown in Figure 1 (as well as in the other optical images) the diffuse gas to the north of E delineates a tail emerging from the A+C complex. Although member E seems to be part of that tail due to its location, its different kinematics suggests that perhaps it does not form part (at least kinematically) of it. On the other hand, from the images and the results in Figure 8, it is apparent that member H seems kinematically to be an extension of the aforementioned tail. If we inspect the velocity pattern of H in Figure 8c, we can see that its peculiar positive velocity can be interpreted as an extension to slightly higher positive velocities of the velocity distribution we see in PA 133° at the north of E. These indications suggest that the faint

tidal tail emerging from the southwest of A+C is bending away from us. This tail curves towards the line that connects with members F and G and comprises the faint ionized gas around member E and the faint zone H. Member E could be an independent kinematical entity.

The slit positions at PA 133° and PA 128°, indicate that the brightest part of members F1 and F2 do not show important velocity gradients. PA 133°, which was selected to cover precisely the main axis that connects both knots, shows a sinusoidal behavior although this is not seen in the other position angle. In PA 128° (which does not cover exactly the nucleus of F2) we see an apparent streaming motion towards positive radial velocities of the faint ionized gas at the north of F1. This streaming motion seems to connect with the southern tip of H. In any case, F1 and F2 seem to be kinematically different to the tidal tail that emerges from the southwest of the A+C complex. It is interesting to note that the average radial velocities of members E and F are quite similar, although they are relatively distant objects within the group. Their velocities are consistent with those expected from their location in the H I velocity maps obtained by Williams et al. (1991). Both objects are located in a zone where the velocity of the neutral gas is rather constant.

Finally, member G was covered by PA 133°. The morphology of this galaxy indicates that it is a small disk galaxy seen nearly face-on. It shows a linear velocity gradient, with the radial velocity increasing towards the northwest. The amplitude of the velocity variation is of about 50 km s⁻¹. This behavior indicates that this galaxy is in solid-body rotation. The velocity map of member G obtained by Richer et al. (2003) shows a similar velocity gradient in this object; the radial velocity increases from the southeast to the northwest.

4. Discussion

4.1. Ages of the bursts and stellar populations

The first determination of the age of the main burst of HCG 31 was performed by Rubin et al. (1990). Assuming that WR stars are not contributing to the ionization of the gas, they found that $N(\text{WR})/N(\text{OB}) \sim 5$. From this ratio, those authors suggested that this burst of star formation

occurred 10 Myr ago and is rapidly declining at the present. IV97 determined the ages of the bursts making use of $(U-B)$ versus $(V-I)$ star formation diagrams combined with the population synthesis models for instantaneous bursts described by Leitherer & Heckman (1995). They found an age between 3.16 and 10 Myr for the youngest bursts, but also detected an old underlying stellar population in some areas. IV97 also studied the $H\alpha$ versus U diagram detecting two bursts in A+C and B: one about 10 Myr old, related to normal star formation activity, and other slightly younger due to star formation during the interaction. A similar behavior was also seen in member G. IV97 suggested that E is a young member, but that the SFR has been decreasing in it for the last 10 Myr. For these authors, member F shows an age almost coincident with the age of the youngest bursts in A+C and B; this object might have been created recently from gas ejected during the interaction.

IV97 concluded that the most remarkable point is that the youngest episode in all galaxies is almost simultaneous, implying that it could have been triggered by the interaction between galaxies A and C. In this way, they suggested that two episodes of star formation have occurred in HCG 31: the youngest one seems to be the dominant in A+C and F; the oldest one in E, and the contribution of both episodes seems to be the same for B and G.

$H\alpha$ emission traces recent star formation activity. $W(H\alpha)$ can be used to estimate the ages of recent episodes of star formation (e.g. Leitherer & Heckman 1995), since it decreases with time. Johnson & Conti (2000) compared the observed $W(H\alpha)$ with the predictions of Leitherer & Heckman (1995) models. They found that the $W(H\alpha)$ sources are very young (less than 10 Myr), with a peak in the distribution corresponding to ages of about 5 Myr. A+C, B, and G show signs of star formation over the past 10 Myr, showing a peak in 5 Myr. They also reported that B shows a second peak at about 10 Myrs, E shows young (1–3 Myr) star formation and an older population similar to the other members, but F has only very strong $W(H\alpha)$, indicating an age below 4 Myr.

We have combined our broad-band optical and NIR photometric values with STARBURST99 (Leitherer et al. 1999) models to estimate the age of the bursts. We have chosen two different spec-

tral synthesis models, both for an instantaneous burst with a Salpeter IMF, a total mass of $10^6 M_{\odot}$ and a $100 M_{\odot}$ upper mass, but with two different metallicities: $Z/Z_{\odot}=0.4$, and $Z/Z_{\odot}=0.2$. The metallicities we derive from the O abundance in the different objects (see Table 5) indicate that this metallicity range should provide a good fit.

Young bursts of star formation are expected to have very negative $U - B$ colors, and most of the luminosity in both bands should come from the massive star populations. Therefore, $(U - B)$ can be used as a very convenient age estimator of the youngest stars. In this way, we have estimated the age of the different galaxies and zones of HCG 31 comparing their $U - B$ color and the results of STARBURST 99 (Leitherer et al. 1999) selected models. The estimated ages are shown in Table 6. It should be remarked that with our spectroscopical data we have obtained a direct determination of the interstellar reddening for most of the galaxies of the group. This allows us to break the age-reddening degeneration in the broadband color-color diagrams (see Johnson et al. 1999). We have found that members D and Q show the highest $(U - B)$ values: they are basically old galaxies, with an age >500 Myr, without evidences of intense ongoing star formation. On the other hand, the objects with the lowest $(U - B)$ colors are F1 and F2. Therefore, they can be interpreted as the youngest objects of the group, with ages lower than 5 Myr. There is not a unique solution for the age of the rest of the objects due to the sinusoidal behavior of the $(U - B)$ color-age relation obtained from the models. We can try to solve this ambiguity making use of a color-color diagram plotting the observed values of $(U - B)$ versus $(B - V)$ and comparing with the theoretical models from 1 to 20 Myr (Fig. 9a). We can note that the observational points fit the models fairly well, providing (in principle) a good age determination. Again, F1 and F2 seem undoubtedly to be the youngest objects. Unfortunately, we cannot still disentangle the age ambiguity in the zone with $(U - B) \leq -0.6$ and $(B - V) \geq -0.1$, the zone where most of the observational data lie. The lack of substantial departures in the position of the observational data with respect to the theoretical positions for single burst models indicate that the contamination of the $(U - B)$ and $(B - V)$ colors by underlying older stellar populations is not rel-

evant. In fact, this is directly reflected in the very good agreement between the ages estimated from the $(U - B)$ color alone and the $(U - B)$ versus $(B - V)$ diagram.

We have also used the NIR colors to obtain independent age estimations and to explore the presence of underlying older populations. It is well known that NIR colors are very good indicators of the stellar population age once the metallicity is fixed (e.g. Vanzi et al. 2000; Vanzi, Hunt & Thuan 2002). Evolutionary synthesis models (as those of STARBURST 99 and others) show that the NIR colors of young populations differ significantly from those of older ones. We have used the $(V - J)$ color as an age indicator and the results are given in Table 6. It is remarkable that objects F1 and F2 give again the lowest values, in agreement with the previous determinations. Again, Q and D seem to be old systems, with colors indicating ages larger than 100 Myr. In Figure 9b we plot the NIR colors $(J - H)$ versus $(H - K_S)$ of the observed objects and the results of STARBURST 99 models for bursts at different ages. The $(J - H)$ colors of the star-forming galaxies of HCG 31 are clearly those expected for young populations, since values of the order of 0.5-0.6 are the typical ones of evolved populations (Vanzi et al. 2002). To compare the colors of the galaxies with the models it is necessary to correct the observations for ionized gas line emission, since STARBURST 99 only considers the contribution of the nebular continuum. We have estimated an average value of the emission line contribution using the results for 24 starbursts by Calzetti (1997) following the NIR study of 3 WR galaxies by Vanzi et al. (2002). An arrow at the right-upper corner of Figure 9b shows this average contribution. As in the previous diagrams, the observational data are again in quite a good agreement with the models, indicating the remarkably small contribution of the old underlying stellar populations and the nebular line emission. In fact, the ages derived for each object from the $(J - H)$ versus $(H - K_S)$ diagram are in very good agreement with those obtained from optical indicators.

Our spectroscopical data can be used to obtain additional independent age indicators. We have used the models by Stasińska & Leitherer (1996) of H II regions, ionized by an evolving starburst embedded in a gas cloud of the same metallicity, to es-

Table 6: Age estimations of the bursts in HCG 31

Method	A	B	C	E	F1	F2	G	H	Q & D	Ref.
H α vs. U	3–10	~ 10	3–10	~ 10	3–10	...	~ 10	IV97
(V vs. I)+W(H α)	~ 5	5–10	~ 5	1–3	< 4	...	~ 5	JC00 ^d
W(H β) ^a	6.5 ± 1.5	7 ± 1	5 ± 1	5.5 ± 1.5	2.5 ± 0.5	2.5 ± 0.5	7 ± 1	4.5 ± 1.5	...	TW ^e
W([O III]) ^a	6.5 ± 1.5	7 ± 1	4.5 ± 1.5	6 ± 1	2.5 ± 0.5	2.5 ± 0.5	5 ± 1	4.5 ± 1.5	...	TW ^e
W(H β) ^b	7 ± 1	7 ± 1	4.5 ± 0.5	5.5 ± 1.5	2.5 ± 0.5	2.5 ± 0.5	5 ± 1	4 ± 1	...	TW ^e
($U - B$) ^c	7.5 ± 3.5	7.5 ± 3.5	8.5 ± 3.5	8 ± 3	3.5 ± 0.5	3.5 ± 0.5	8.5 ± 3.5	...	> 500	TW ^e
($B - V$) vs. ($U - B$) ^c	10.5 ± 4.5	10 ± 5	10.5 ± 4.5	10.5 ± 4.5	4 ± 1	4 ± 1	10.5 ± 4.5	TW ^e
($V - R$) ^c	6.5 ± 1.5	7 ± 1	6 ± 1	7 ± 1	3 ± 1	3 ± 1	7 ± 1	...	> 100	TW ^e
($V - J$) ^c	9 ± 2	6.5 ± 1.5	7 ± 1	6.5 ± 0.5	3 ± 0.5	4.5 ± 0.5	7 ± 1	...	> 100	TW ^e
($J - H$) vs. ($H - K_S$) ^c	7.5 ± 0.5	7 ± 1	4.5 ± 0.5	5.5 ± 1.5	3.5 ± 0.5	4.5 ± 0.5	7 ± 1	TW ^e
Estimated age (Myr)	7 ± 1	7 ± 1	5 ± 1	6 ± 1	2.5 ± 0.5	2.5 ± 0.5	6 ± 1	4 ± 1	> 500	TW ^e

^aStasińska & Leitherer (1996) models.

^bSchaerer & Vacca (1998) WR galaxies models.

^cSTARBURST 99 (Leitherer et al. 1999) models.

^dJohnson & Conti (2000) using HST data.

^eThis Work.

timate the ages of the bursts. We have chosen two models, both with metallicity $Z/Z_{\odot} = 0.25$, and with a total mass of $M/M_{\odot} = 10^3$ and 10^6 . In Figure 10 we plot our observational values of $W(H\beta)$ and the $[O III] \lambda 5007/H\beta$ emission line flux (see Tables 3 and 4) and compare them with the theoretical models. All the objects show an excellent fit except member B, which has the strongest contribution of the underlying stellar continuum in the spectrum. As for the rest of the indicators, objects F1 and F2 are the youngest bursts. In Table 6, we also include the age estimations obtained from the comparison of the observed values of $W(H\beta)$ and $W([O III])$ and the results of the models by Stasińska & Leitherer (1996). The fact that both indicators show similar ages indicates that the underlying stellar continuum has a very limited effect on the measured $W(H\beta)$. We have also used the models by Schaerer & Vacca (1998). In Table 6, we also include the age estimations obtained using these last models and the observed values of $W(H\beta)$. As it can be seen, the ages obtained using both models are in excellent agreement.

We have included our final adopted age estimation for each object in the last row of Table 6. This estimation is the most probable value taking into account the indicators that are characteristic of the emission from massive star populations: $W(H\beta)$, $W([O III])$, and the $(U - B)$ color. We can see that, undoubtedly, objects F1 and F2 have the youngest bursts, with ages between 2 and 3 Myr.

Member H also seems to be a very young object, but the low signal-to-noise ratio of its spectrum does not permit us to be confident on this. Members A, B, E, and G show ages between 5 and 8 Myr in their bursts, whilst the brightest object of the group, member C, shows an age between those bursts and the younger F1 and F2. We think that it is significant the consistency of the age estimations obtained making use of different theoretical models and very different indicators obtained from independent kinds of data: optical imaging, NIR imaging, and optical spectroscopy. This indicates the remarkably small contribution of the underlying old stellar populations and the robustness of the actual knowledge about starbursts and the models available for their analysis. This can be graphically demonstrated in the good agreement between photometric and spectroscopy data, as we show in Figure 11, where we plot our observational values of $W(H\beta)$ versus $(U - B)$, finding a very good agreement with STARBURST 99 (Leitherer et al. 1999) predictions.

We have analyzed the surface brightness profiles of members A+C, E, F1, F2, and G in order to study the spatial distribution of their different stellar populations and to look for an underlying old component. We have taken concentric surfaces at different radii from the centre of each system, and calculated the integrated flux inside each circle of area A using the relation:

$$\mu_X = m_X + 2.5 \log A, \quad (6)$$

Table 7: Structural parameters of some galaxies in HCG 31.

Member	U.C. ^a	$\mu_{V,0}$	α_V (kpc)
A+C	yes	21.66	2.38
E	?	22.12	0.82
F1	no	22.25	0.56
F2	no	23.43	2.52
G	?	21.52	1.58

^aUnderlying component.

to obtain the surface brightness, μ (in units of mag arcsec²), of each circle A (in units of arcsec²) in each filter X (U , B , V and J), m_X is the magnitude in the filter X . In Figure 12 we present the surface brightness for U , B , V and J filters versus the size of the aperture (in arcsec) for A+C, G, E, and F1. The dotted vertical line is the average seeing. This analysis is not precise for the study of irregular morphologies like those of B and A+C, but it is useful for our main purpose and it is valid for approximately circular compact objects like E, F1, and F2. A detailed study on surface brightness profiles can be found in Cairós et al. (2001). These authors perform such a study for a sample of blue compact dwarf galaxies, which included several members of HCG 31: Mrk 1089 (A+C complex) and Mrk 1090 (member G). Cairós et al. find that the A+C complex presents an exponential profile, whereas member G shows a reasonable fit to both exponential and de Vaucouleurs profiles. In the majority of the observed galaxies, Cairós et al. find a low surface brightness component underlying the contribution of the starburst, but they do not observe this in the case of the galaxies of HCG 31.

In Figure 12 we also show the radial color profiles ($U - B$), ($B - V$) and ($V - J$) derived by a direct subtraction of two light profiles. The color profiles cannot be used to detect small variations in the inner regions of the galaxy, but they are useful for describing the color variation as a function of the distance. In these graphics we also indicate the representative average color derived for each system (see Table 2) by a dotted horizontal line. Thus, this line shows the color within the 3σ radio that we used for the aperture photometry. We have centered the radial profile in

A+C just between the two brilliant central knots (see Fig. 1). In Figure 12 we can see that A+C has a low surface brightness component underlying the burst since the surface brightness profile can be separated in two components, a disk structure and the contribution of the starburst. This underlying component was not detected by Cairós et al. (2001), but it can also be observed in the ($U - B$) and ($V - J$) color profiles. We have performed an exponential law fitting to the V profile, following the expression:

$$I = I_0 \exp(-\alpha r), \quad (7)$$

that describes a typical disk structure: I_0 is the central intensity and α is the scale length. The fitting structural parameters are indicated in Table 7 and the fit is plotted over each V profile in Figure 12 with a straight line. In member G the fitting is fairly good, and this suggests that G has not an important underlying old component. However, the color profiles, specially ($V - J$), show a strange behavior, that can be explained noticing that the starbursts in G are not located at the center of the galaxy, but in its northwest side (see Fig. 1). E could possess a very faint underlying component, but we cannot confirm it. The exponential fitting for this member was only performed for radii larger than the one considered for the optical photometry. Finally, we do not detect low brightness underlying components in F1 and F2 in the optical filters (we have also included in Figure 12 the R profile for F1 and its linear fitting). It can be seen that the old stellar population is not significant in these objects, which are clearly dominated by the starburst. This fact is in very good agreement with our age estimation for them (see Table 6). Johnson & Conti (2000) also remarked that F1 and F2 were the only members in HCG 31 that did not show old populations. However, following the recent study by Noeske et al. (2003), a probable old population could be found if F1 and F2 were studied using high spatial resolution photometry in NIR, because the starburst emission overshines the underlying population in the inner part of the objects in the optical wavelengths. Nevertheless, we argue that F1 and F2 seem to be *really* very young and recently-formed objects, and that the relative contribution of an hypothetical old population, if any, should be very small.

4.2. WR population

We have used evolutionary synthesis models by Schaerer & Vacca (1998) for O and WR populations in young starburst to estimate the number of O and WR stars in F1 and F2. We have assumed that $L(H\beta)=4.76\times10^{36}$ erg s $^{-1}$ for a O7V star and $L(WNL\ 4686)=1.7\times10^{36}$ erg s $^{-1}$ for a WNL star (Vacca & Conti 1992). The extinction-corrected flux of the broad He II $\lambda 4686$ emission line is 4.69×10^{-17} erg cm $^{-2}$ s $^{-1}$ for F1 and 2.26×10^{-17} erg cm $^{-2}$ s $^{-1}$ for F2 (see Table 8). However, we must correct these values for the size of the slit with respect to the true area of each member. From the photometric values, we have adopted a ratio of 4 for F1 and 2 for F2. Taking into account a distance of 54.8 Mpc for HCG 31, we obtain a luminosity for the He II $\lambda 4686$ line of about 4.27×10^{39} erg s $^{-1}$ for F1 and 1.71×10^{39} erg s $^{-1}$ for F2. If we assume that all the contribution in the He II $\lambda 4686$ emission line comes from WNL stars, we obtain around 40 and 10 WR stars in F1 and F2, respectively. From the $H\beta$ flux, correcting the contribution of the WR stars to the ionizing flux, and the contribution from other O stars (we have derived that $\eta \equiv O7V/O=0.25$ for C and $\eta=0.5$ for F1 and F2 using the estimated age derived for each burst, see Figure 21 in Schaerer & Vacca 1998), we finally obtain about 1660 and 680 O stars and a WR/(WR+O) ratio of 0.024 and 0.014 for F1 and F2, respectively.

We have also performed a similar analysis for C. We obtain a WR/(WR+O) ratio of 0.003. This value is similar to the one of 0.005 estimated by Guseva et al. (2000).

We show all the observed and derived WR population values for C, F1 and F2 in Table 8. We have compared these results with the predictions from Schaerer & Vacca (1998) models for O and WR populations in young starbursts. In Figure 13a we plot the He II $\lambda 4686$ emission line flux versus the $H\beta$ equivalent width for the models with 0.4 and 0.2 Z_{\odot} . We observe that F1 and F2 show quite a good agreement with these models, but C does not. This difference between the observed and predicted values in C seems to be real, because Guseva et al. (2000) obtain a similar WR/(WR+O) ratio. The difference could be due to aperture effects. Perhaps, the area observed inside the A+C complex does not comprise the

WR-rich area. This effect is not important in F1 and F2 because of their small size. Very probably, we are measuring all the emission from the WR stars located in these bursts.

In Table 8 we also include the WR/(WR+O) ratio obtained using two different calibrations by Schaerer & Vacca (1998): one from the blue WR bump flux (and their eq. 17) and other derived, only for C, from the He II $\lambda 1640$ emission line equivalent width (and their eq. 18). We have assumed that all the blue WR bump flux comes from the He II $\lambda 4686$ emission line. We find a good agreement for F1 and F2, but not for C. We have also used the W(He II) $\lambda 1640$ obtained from HST UV spectroscopy by Johnson et al. (1999) for C, and the calibration derived by Schaerer & Vacca (1998) for this particular emission line (their eq. 18), and find WR/(WR+O) ≈ 0.057 , one order of magnitude higher than our estimations using the blue bump flux and the one by Guseva et al. (2000). This value, that is in better agreement with the theoretical predictions, is plotted with a triangle in Figure 13b. The difference between the UV and optical values can be due to the fact that the UV spectrum was obtained from HST observations of the bright knots of the A+C complex, precisely the regions where the WR stars and the highest SFRs are found. Therefore, these determinations based on the W(He II) $\lambda 1640$ should be less affected by aperture effects.

4.3. Star formation rates

We can use the $H\alpha$ emission to calculate the SFR in each burst of HCG 31. IV97 presented the $H\alpha$ luminosities obtained from CCD imagery for all the members in HCG 31. We have used their data and the Kennicutt (1998) calibration:

$$SFR_{H\alpha} = 7.94 \times 10^{-42} L(H\alpha), \quad (8)$$

to estimate the SFR (in units of M_{\odot} yr $^{-1}$) in the most important members from $L(H\alpha)$ (in units of erg s $^{-1}$). But we have to correct their data from several contributions. First, we correct by the different distance assumed for HCG 31 (IV97 considered that the compact group was at 41.23 Mpc whereas we are using a distance of 54.8 Mpc). Then, we must also correct the data for the reddening that we have derived for each burst. Finally, we correct for the contribution of [N II] emission to the total $H\alpha$ flux taking into account our

Table 8: Analysis of O and WR populations in C, F1, and F2.

	C	F1	F2
$F(\text{He II } \lambda 4686)^a$	2.04×10^{-16}	4.69×10^{-17}	2.26×10^{-17}
$W(\text{He II } \lambda 4686) \text{ (}\AA\text{)}$	0.34 ± 0.07	2.66 ± 0.5	2.03 ± 0.6
Slit size correction	7.3	4	2
Size (kpc^2)	6.43	0.98	0.49
η	0.25	0.50	0.50
WNL stars	300	40	10
O stars	96600	1660	680
WR/(WR+O)	0.003	0.024	0.014
WR/(WR+O) ^b	0.008	0.022	0.015
WR/(WR+O) ^c	0.057

^aIn units of $\text{erg s}^{-1} \text{ cm}^{-2}$.

^bBased on our determinations of the blue WR bump flux.

^cBased on the $W(\text{He II } \lambda 1640)$ obtained by Johnson et al. (1999).

spectroscopic data. That contribution represents between 5 and 15 % of the narrow $\text{H}\alpha$ filter total flux. We show the corrected $\text{H}\alpha$ luminosity and the SFRs derived from them in Table 9.

We have also estimated the SFR from the $\text{H}\alpha$ luminosity provided by our spectra for comparison. We have considered the slit size with respect to the whole area in each burst to estimate the total luminosity (r factor in Table 9). We include the results obtained by this method in Table 9, as well as the SFR per kpc, that was calculated dividing the SFR by the total area, A , of the observed burst. We note that there is a good general agreement between both methods, although the results derived from the IV97 data are systematically higher by a factor of 2. As we could expect, the highest SFR is found at the center of the A+C complex, with $4.77 M_{\odot} \text{ yr}^{-1}$ (from the IV97 data) and $2.74 M_{\odot} \text{ yr}^{-1}$ (the spectroscopic value). We can compare these values with the SFR derived from the 60 and 100 μm fluxes measured with *IRAS* (Moshir et al. 1990). Moshir et al. found $f_{60}=3.920 \text{ Jy}$ and $f_{100}=5.840 \text{ Jy}$. Using the Kennicutt (1998) calibration:

$$SFR_{IR} = 4.5 \times 10^{-44} L_{FIR}, \quad (9)$$

where

$$L_{FIR} = 1.26 \times 10^{-11} (2.58 f_{60} + f_{100}), \quad (10)$$

we find that the SFR derived from infrared fluxes is $SFR_{IR}=3.18 M_{\odot} \text{ yr}^{-1}$, in good agreement with

our estimations from $\text{H}\alpha$ luminosities. We can also remark that C, F1, and F2 are the systems with the highest SFRs when the size of each burst is considered.

4.4. The luminosity-metallicity relation

Richer et al. (2003) used the relation between absolute magnitude and metallicity for dwarf irregular galaxies proposed by Richer & McCall (1995) for the HCG 31 members, finding that the position of A and C is rather unusual. In fact, these objects seem to be too luminous for their oxygen abundances. In Figure 14, we show the luminosity-metallicity relation we obtain for the objects as well as the Richer & McCall (1995) relation for comparison (as in Richer et al. 2003, with an extrapolation to higher luminosities). Our O/H ratios are quite similar to those adopted by Richer et al. (2003) for members C and F. In the case of member B our determination is 0.2 dex lower than that obtained by Richer et al. (2003) and now is similar to the abundances of the rest of the brightest objects of the group. In the case of member A, we only have an indirect estimation of the O/H ratio of A1 based on empirical methods. Taking into account the systematic larger abundances that we obtain with the empirical methods for all the objects (see § 3.3.2), we prefer to use the direct determination of O/H obtained by Izotov & Thuan (1998) as representative for A. With this abundance, the position of A is similar to the

Table 9: Star formation rates for HCG 31 bursts.

Member	$\log L(\text{H}\alpha)$	SFR ($M_{\odot} \text{ yr}^{-1}$)	SFR ($M_{\odot} \text{ yr}^{-1} \text{ kpc}^{-1}$) ^a	Reference ^b
A+C	41.78	4.77	...	IV97 adapted
A+C inner part	41.54	2.74	0.43	Spec, $r = 7.3$, $A = 6.43 \text{ kpc}^2$
A1	38.76	0.005	0.01	Spec, $r = 2$, $A = 0.42 \text{ kpc}^2$
B	40.22	0.13	0.04	Spec, $r = 6$, $A = 2.94 \text{ kpc}^2$
E	40.50	0.27	...	IV97 adapted
E	40.05	0.09	0.05	Spec, $r = 7$, $A = 1.715 \text{ kpc}^2$
F1	40.40	0.20	...	IV97 adapted
F1	40.12	0.10	0.10	Spec, $r = 4$, $A = 0.98 \text{ kpc}^2$
F2	40.09	0.10	...	IV97 adapted
F2	39.67	0.04	0.08	Spec, $r = 2$, $A = 0.49 \text{ kpc}^2$
G	40.75	0.41	...	IV97 adapted
G	40.60	0.31	0.06	Spec, $r = 10$, $A = 4.9 \text{ kpc}^2$
H	38.17	0.001	0.015	Spec, $r = 1$, $A = 0.26 \text{ kpc}^2$

^aDerived considering the SFR shown in column 3 and the total area A of the burst shown in column 5.

^bThe r parameter shows the ratio between the total area of the burst and the area covered by the slit.

other objects on the diagram. The position of object H in the diagram is very uncertain because we only have a lower limit for its absolute magnitude and the O/H ratio has also been estimated from empirical calibrations.

In Figure 14, we can see that the unusual position of A and C in the luminosity-metallicity relation found previously by Richer et al. (2003) is also a property of the other bright galaxies of the group: B and G. Therefore, members A, B, C, and G (the four brightest galaxies of the HCG 31 group) show rather similar O/H ratios ($12+\log(\text{O}/\text{H}) = 8.0\text{--}8.2$), about 0.3 dex (a factor of 2) lower than the value expected from the Richer & McCall (1995) relation. We consider that this is a real behavior because the abundances are well determined, based on the direct measurement of the electron temperature for most of the objects. In addition, as we have commented above, our abundances are similar to previous determinations for those objects with data available in the literature. The systematical offset of the objects in the luminosity-metallicity relation can also be explained by a displacement of about 2 magnitudes in the magnitude axis. This amount seems too large to be accounted for by observational errors. Our absolute magnitudes are similar to those obtained in previous works (see Richer et al. 2003) and the colors derived (even comparing optical and NIR data) do not show any systematic trend that could suggest the presence of calibration problems.

The apparently unusual position of the brightest galaxies of HCG 31 in the luminosity-metallicity relation deserves further discussion. Richer et al. (2003) interpreted the unusual positions they found for galaxies A and C as the combination of dilution due to strong gas inflow (arising from the funneling of the gas towards the central zones due to interactions) and the transient high luminosity due to the strong star formation. Taking into account our results, the explanation proposed by Richer et al. (2003) based on inflows seems unlikely. It is difficult to understand how the four galaxies could experience gas inflows in a manner that produce similar final abundances in all the objects. The four galaxies are located in different positions inside the group and have different physical characteristics; therefore, the properties and intensities of the hypothetical inflows should be different. It is clear that the ultimate reason of the abnormal positions in the luminosity-metallicity relation should explain the position of all the four objects. We have to take into account that the luminosity-metallicity relation used by Richer et al. (2003) (as well as the previous one obtained by Skillman, Kennicutt & Hodge 1989) has been obtained for local dwarf irregular galaxies, with $M_B \geq -18$ (the most common upper limit for the brightness of a dwarf galaxy). All the galaxies with the "unusual" position are brighter than this limit and therefore cannot strictly be considered dwarf galaxies, especially C, which is about 1.5 magnitudes brighter than that limit. In

fact, Richer et al. (2003) indicate that member C has a luminosity like that of a typical late-type spiral galaxy, and also that its position in the luminosity-metallicity relation is compatible with the extreme low end of the abundance range of late-type spirals (Garnett et al. 1997). However, we think that the O abundance of member C is more consistent with the expected abundance in the external zones of spiral galaxies of the same luminosity (see Garnett et al. 1997; their Figure 18). We have derived the O abundance in the brightest part of C, which should correspond to the nucleus of the galaxy. Therefore, the correct comparison would be with a relation between luminosity and central abundances, as it is shown in Figure 16 of Garnett et al. (1997). In this case, member C, as well as the other three bright galaxies of the group are located between 0.5 and 1 dex below the central abundances reported by Garnett et al. (1997). In any case, the O/H ratios of the brightest members of HCG 31 are more consistent with those found in Magellanic-type irregular galaxies.

Several authors have questioned the validity of the luminosity-metallicity relation of dwarf galaxies. Campos-Aguilar et al. (1993) and Peña & Ayala (1993) find no evident relation for blue compact galaxies, and McGaugh (1994) does not support such relationship for low surface brightness galaxies. Therefore, the luminosity-metallicity relation may be not valid for gas-rich galaxies. In particular, HCG 31 should be considered as a gas-rich group because its global $L_B/M(\text{H I})$ is approximately unity taking into account a total hydrogen mass of $2.1 \times 10^{10} M_\odot$ (Williams et al. 1991). Chemical evolutionary models by Hidalgo-Gómez, Sánchez-Salcedo & Olofsson (2003) indicate that a linear correlation between luminosity and metallicity could be feasible for non-bursting dwarf irregular galaxies, but that a plateau is reached at about $M_B \leq -18$, just at the limit of the definition of a dwarf galaxy. This can be seen graphically in the Figure 8 of Hidalgo-Gómez et al. (2003), where their most luminous model galaxies are located at $12 + \log(\text{O}/\text{H}) \simeq 8.1$, precisely the abundance of the brightest members of HCG 31. Other interesting conclusion of Hidalgo-Gómez et al. (2003) is that variations in the stellar mass-to-light ratio can contribute significantly to the scatter in the luminosity-metallicity relation. This was first pointed out by Peña & Ayala (1993), who interpret

the lack of correlation between the B -luminosity and metallicity of their sample of H II galaxies as the transient increase of luminosity due to the intense starburst that these objects are experiencing. Peña & Ayala propose that, once the bursts evolve, the position of these galaxies will move toward lower luminosities, perhaps approaching the luminosity-metallicity relation of non-bursting dwarf irregulars. In fact, Hidalgo-Gómez & Olofsson (1998) propose that perhaps NIR magnitude is a more suitable transient indicator, taking into account the contribution of the starburst to the B -magnitude.

We have further explored the effect of the onset of the starbursts on the absolute B -magnitude of a galaxy. In Figure 15 we show the evolution of M_B versus time for a $Z/Z_\odot = 0.2$ burst as predicted by the population synthesis models of STARBURST 99 (Leitherer et al. 1999). We have considered a $10^6 M_\odot$ instantaneous burst and three different stellar mass distributions: a) Salpeter IMF and $100 M_\odot$ upper mass; b) Salpeter IMF and $30 M_\odot$ upper mass; c) stepper IMF ($\alpha = 3.30$) and $100 M_\odot$ upper mass. We consider that case (a) could be more appropriate for the galaxies of HCG 31. In fact, as Emelgreen, Kauffman & Thomasson (1993) indicate, massive star formation in interacting galaxies may have a higher efficiency than in other scenarios, and the clouds should have larger internal temperatures, producing the shift in the stellar mass function toward more massive stars. On the other hand, as Johnson et al. (1999) and Johnson & Conti (2000) demonstrated, the starbursts of NGC 1741 and other members of HCG 31 are composed by a large number of SSCs. The masses of those clusters range between 10^4 and $10^6 M_\odot$, so the B -magnitude evolution of the galaxies should be represented as a combination of a number of clusters evolving as shown in Figure 15. The different curves clearly indicate that the B -magnitude of the burst could be increased in several magnitudes during the first 10 Myr with respect to the brightness in the quiescent phase. This effect is surely affecting the positions of the galaxies of HCG 31 shown in Figure 14 because their blue luminosities are dominated by young, almost coeval, starbursts. In the future, the positions of the brightest galaxies (A, B, C, and G) will be shifted toward the right on the diagram in their evolution toward

the quiescent phase; eventually reaching positions nearer the metallicity-luminosity relation. In this case, it is even possible that some of these galaxies could be classified as bona-fide dwarfs.

Summarizing, the members of HCG 31 are dominated by strong and very young starbursts with ages below 10 Myr. We consider that the emission of this short-lived young stellar population is increasing so intensely their B -luminosity that the use of the metallicity-luminosity relation is no longer appropriate for these objects. In accord with other previous suggestions, we propose that the use of this relation is not appropriate for starburst-dominated galaxies.

4.5. Are E and F Tidal Dwarf Galaxies?

In contrast with what happens for the brightest galaxies, the position of objects E and F1 in the O/H versus M_B diagram (Figure 14) seems to be rather consistent with the metallicity-luminosity relation. However, we think that this could be fortuitous. Taking into account the conclusion of the previous section, the very blue colors and small sizes of those objects imply that the contribution of the young population should be even more important than in the brightest galaxies of the group. Probably, the future photometric evolution of their starbursts will move their positions toward lower luminosities, away from the relation, after the first 10 Myr. If this prediction is correct, it favors their tidal dwarf nature, as several authors have pointed out previously. As it was commented above, the O/H ratios of E, F1, and F2 are of the order of the values obtained for the brightest members of HCG 31 despite their different luminosities and distances to the A+C complex. Moreover, E, F1, and F2 have also N/O ratios (considering $N/O \approx N^+/O^+$) similar to those of the brightest galaxies within the uncertainties (see Table 5). This is remarkable, because the bulk of N is thought to be produced by intermediate mass stars, indicating that the material shows some degree of contamination of previous populations. This fact favors that the galaxies are not made of pristine clouds but instead of material stripped from other chemically evolved galaxies.

Tidal dwarf galaxies (TDGs) are thought to be built from the outer disks of their parent galaxies. Weibacher, Duc & Alvensleben (2003) present results for a large number of TDG candidates in a

sample of interacting galaxies. These authors indicate that their TDG candidates are likely to contain a significant amount of old stars, and that the tidal tails located at different distances of the same parent galaxy do not show evidences of abundance gradients along the tails. In the case of members E and F, we do not see clear abundance differences within the uncertainties, and the presence of older population does not seem to be important. The absence of differences in the O/H ratios between the brightest objects, specially the A+C complex, and members E and F, is remarkable in this sense. If E and F are in fact TDGs of one of the brightest galaxies of the group (member A or C) and the progenitor was a spiral (with an abundance gradient), they should show lower O/H ratios than the nucleus of the parent galaxy. This result favors that the progenitor is probably an irregular galaxy with an homogeneous abundance across its volume.

Weibacher et al. (2003) obtained a mean $12+\log(O/H)=8.34\pm0.14$ for their sample of TDGs candidates. The O/H ratios of E, F1, and F2 (around 8.1) are compatible with the lower end of that range of values, but are higher than the abundances of the three objects that Weibacher et al. (2003) interpret as pre-existent dwarf companion galaxies ($12+\log(O/H)$ between 7.6 and 7.8). A pre-existent dwarf galaxy should have an oxygen abundance compatible with the metallicity-luminosity relation studied before. If members E, F1 and F2 in HCG 31 were pre-existent dwarf galaxies, following this relation they would have metallicities around 0.5 dex lower than the brightest galaxies of the group (between 7.6 and 7.7), but these values are not observed. On the other hand, Weibacher & Duc (2001) and Weibacher et al. (2003) indicate that the three pre-existent companions seem to contain a strong old stellar component, property that is not observed in objects E, F1, and F2 either.

Normal dwarf galaxies are stable entities with their own dynamics, so the best definition of a TDG is that it behaves as a self-gravitating object (Duc et al. 2000; Weibacher & Duc 2001). To confirm if a knot in a tail is a genuine TDG we have to know the kinematics of the knot. Weibacher et al. (2003) interpret a knot as a TDG candidate when it shows a kinematics decoupled from the expanding motion of the tidal tail, and

possibly rotation. In Figure 8, we can see that the faint optical tidal tail that emerges from the southwest of member C shows a linear continuous tidal streaming motion just at the north of member E, with velocities ranging from -100 to $+50$ km s^{-1} from its base to object H. However, as it can be seen in Figure 8b, member E shows a velocity pattern very different from the kinematical behavior of the tidal tail. This fact indicates two possibilities: E does not belong to the faint optical tidal tail or is a TDG decoupled from the tail. The velocity patterns of objects F1 and F2 are also rather constant and very different from those found in the optical tidal tail, especially in the apparent tip, object H. However, there is not clear evidence of rotation patterns in the velocity distributions inside objects F1 and F2.

As we have commented in section 3.3.4, the mean velocities of objects F1 and F2 are similar to those of members E and G, which coincide with the radial velocity of the H I cloud in this part of HCG 31. This fact suggests that perhaps E, F1, and F2 are related to the arm-like H I structure that extends to the southeast of the A+C complex. We think that the velocity pattern and the morphology of the system are compatible with the presence of two spatially coincident kinematical structures:

- the arm-like H I structure that extends from A+C in direction to member G, from which objects E and F may have formed, and showing a rather constant radial velocity;
- the optical tidal tail that emerges from the southwest of the A+C complex, which consist of a curved string of faint star-forming regions that seems to end at the position of object H (see Fig. 1). It shows a clear streaming motion bending away from us.

We propose that objects E, F1, and F2 are TDGs made from material in the southern arm-like H I extension, which was stripped from the parent galaxy, probably the A+C complex because of the relatively high chemical abundances, very similar to those of the brightest galaxies of the group. The apparent absence of old stellar population in the three objects indicates that they are basically made of gaseous (but chemically evolved) material. In fact, a local maximum in the distribution of H I emission coincides with the position

of member F (Williams et al. 1991). We have estimated that these dwarf objects have a total mass between 10^7 and $10^8 M_{\odot}$, the typical values for dwarf irregular galaxies. Therefore, objects E, F1, and F2 should have formed from gas stripped from the disk of a parent galaxy with a rather flat abundance gradient, perhaps an irregular galaxy.

4.6. The star formation history of HCG 31 revisited

The history and future fate of the HCG 31 system have been discussed by several authors (Rubin et al. 1990; Iglesias-Páramo & Vílchez 1997; Johnson & Conti 2000; Richer et al. 2003). We consider that our new data give some new useful elements that can lead to a better understanding of this amazing interacting system.

As it was commented in §§ 3.1 and 3.3.4, the complex morphology of A+C (double nucleus, presence of stripped disks or tidal tails) and the position-velocity diagram of PA 61° indicate that both galaxies are merging. In fact, this object shows the most intense (and one of the most recent) star formation activity of the group. Moreover, IV97 indicate that the colors of the A+C complex are well reproduced by the models of photometric evolution of mergers of two galaxies of similar morphological type of Fritze-von Alvensleben & Gerhard (1994). O'Halloran et al. (2002) presented maps in 7.7 and $14.3 \mu\text{m}$ and spectrometry of HCG 31 using the Infrared Space Observatory (*ISO*). They detected strong mid-IR emission from the central burst, along with strong polycyclic aromatic hydrocarbon (PAH) features and a blend of other features, including [S IV] at $10.5 \mu\text{m}$. The $14.3/6.75 \mu\text{m}$ and $14.3/7.7 \mu\text{m}$ flux ratios suggest that the central burst within HCG 31 may be moving toward the post-starburst phase. On the other hand, Yun et al. (1997) observed a CO deficiency and a peculiar molecular gas distribution in HCG 31. The brightest CO peak occurs in the overlap region between the galaxies A and C, and the enhanced CO emission and associated star formation may be the result of the ongoing merger. They interpreted the observations with a scenario where the compact group is subject to continuous tidal disruptions. Both tidally induced star formation and tidal stripping may be at work resulting in the reduced molecular gas reserve. This is a very likely situation for

HCG 31 taking into account the different and complex evidences of interaction, merging, and tidal stripping that this system shows. Yun et al. (1997) also found a similar behavior in the CO distribution of HCG 92 (*Stephan's Quintet*).

Galaxy B shows solid-body rotation with an amplitude of about 200 km s^{-1} (see the position-velocity diagram of Rubin et al. 1990, that passes precisely across the major axis of the galaxy), and is counter-rotating with respect to the A+C complex. Our broad-band images, as well as the $H\alpha$ ones of IV97, indicate some physical connection (perhaps a tidal bridge) between B and the A+C complex (this connection is quite obvious in Fig. 1). Richer et al. (2003) describe B as a dwarf spiral or irregular galaxy seen nearly edge-on, but we think that it is a bar-like irregular galaxy, taking into account its morphology in $H\alpha$ (see IV97). It is clear from its nebular emission and very blue colors that galaxy B is experiencing a strong star formation activity. This activity may be related to the interaction with the A+C complex. IV97 found that this galaxy shows two maxima in $H\alpha$ equivalent width located at the northern and southern tips of the galaxy. They suggest that this fact could be related to some kind of stripping mechanism. It is interesting to note that the behavior of galaxy B is quite similar to that of the blue compact dwarf galaxy Mrk 1094 ($M_B = -18.4$). This galaxy has been studied by Méndez et al. (1999) and consists of an ensemble of star-forming knots distributed in a twisted bar-like structure, which also shows two maxima of $W(H\alpha)$ at the tips of the bar. Méndez et al. (1999) propose that the characteristics of Mrk 1094 can be explained if it is interacting with a companion H I cloud located 50 kpc to the south. The models of tidal interactions of disk galaxies of Noguchi & Ishibashi (1986) predict that bars are very likely produced in close encounters. These authors predict that the maximum activity of the bursts produced by the interactions takes place $\sim 3 \times 10^8 \text{ yr}$ after the *perigalacticon* (the time when cloud-cloud collisions become more frequent and the SFR reaches a maximum), which is of the order of the crossing times for galaxies within groups the size of HCG 31 (Rubin et al. 1990). According to Noguchi (1988), the infall of gas toward the nuclear region of the galaxy triggers the SF in the center of the galaxy. Perhaps, the maxima

of $W(H\alpha)$ at the tips is indicating the propagation of the star formation outwards along the bar. As IV97 and Richer et al. (2003) suggest, galaxy B may probably merge with the A+C complex in a short time and is now undergoing the first stages of the interaction process.

As discussed in § 4.5, members E and F seem to be TDGs candidates made of gas from the armlike H I structure. This structure should have originated in the external zones of the galaxies of the A+C complex, since the chemical abundances in E, F, and the A+C complex are very similar. The fact that this H I structure and the optical tidal tail at the southwest of A+C are kinematically decoupled is striking, and indicates that they are different objects. Johnson & Conti (2000) suggest that both the optical tidal tail and the arm-like structure are the same entity and could correspond to the inflow of gas to member G from the direction of the main body of the H I cloud in which HCG 31 is embedded, regardless of the direction of motion of G relative to the ambient gas. This scenario can explain the coincidence of member G with a peak of the H I distribution at the end of the arm-like structure. Richer et al. (2003) propose that a gravitational interaction between member G and the A+C complex is the most complete explanation of the events occurring in HCG 31. For these authors, the star formation processes taking place almost simultaneously in A+C, E, F, and G were produced by the fly-by encounter between A+C and G. Richer et al. (2003) interpret the H I structure as the counterpart of the optical tidal tail, but we have found kinematical evidence that this is unlikely. In this context, the absence of a radial velocity gradient along the arm-like H I structure indicates that the relative motion between G and the A+C complex must be in the plane of the sky. Richer et al. (2003) estimate that the expected range of possible transverse velocities of the gas is of several hundreds of km s^{-1} , and conclude that neither the velocities nor the spatial extension between galaxies G and A+C (40 kpc) are unusual when compared to those found in other well-studied interacting systems.

The presence of two adjacent tails has been reported in other interacting systems, but these reports correspond to bifurcated tails [e.g. M81 (van der Hulst 1979; Yun, Ho & Lo 1994); NGC 3921 (Hibbard & van Gorkom 1996); NGC 2535/6

(Kaufmann et al. 1997); Arp 299 (Hibbard & Yun 1999); NGC 4038/39 (Hibbard et al. 2001)]. For example, in the case of NGC 4038/39 (*The Antennae*) one of the tails is visible in the optical while the other, that runs parallel to the first, emits only in H I and does not show an optical counterpart. Hibbard et al. (2001) interpret the bifurcated tails of NGC 4038/39 as produced by a lateral twist in the tail that may cause the outer edge (gas-rich region) to lie in a different plane from the brighter and gas-poor inner regions. This effect can be exacerbated by a preexisting warp in the progenitor disk. In all the cases with enough kinematical data, bifurcated tails show quite similar kinematics, in contrast to the situation we are seeing in HCG 31, where the southwest optical tail and the arm-like H I structure have different kinematics.

Considering all the observational data available for the group, we propose that there are several simultaneous interaction processes taking place in HCG 31. The fly-by encounter between G and the A+C complex originated the H I tidal tail (arm-like structure). This process perhaps occurred before the merging of A and C because the H I tail is the longest structure in the group. Afterwards, the merging of A and C would create the northeast and southwest optical tidal tails. The triggering of the star formation in galaxy G could be due to the inflow of the material from the H I tidal tail. In fact, the star-forming regions form a U shape along the northwest side of G, precisely in the direction toward the A+C complex. The TDGs candidates E and F have been recently created from interaction-induced instabilities on the H I tidal tail and nowadays they show a strong star formation activity, specially intense in F where WR features are detected. Finally, galaxy B suffers some kind of interaction-induced star formation probably propagating along its bar.

As we can see, HCG 31 is a very complex system where interaction effects are not only between two galaxies. In fact, four galaxies (A, C, B, and G) seem to be involved in different interaction processes. This does not seem to be a common phenomenon in the local universe, but it could be very usual in places with a high density of galaxies, like the early universe, when interactions could occur frequently. Nowadays, hierarchical galaxies formation models (e.g. Kauffman & White 1993) suggest this scenario. The detailed study of systems

like HCG 31 in the local universe could provide important clues about the evolution of galaxies in high density environments.

5. Conclusions

In this paper we present results based on new broad-band optical and near-infrared imagery and optical spectroscopy of the compact group HCG 31. Our main results can be summarized as follows:

- We have obtained remarkably consistent age estimations for the most recent star formation bursts of the group using different observational indicators and theoretical models. Member F hosts the youngest starburst of the group (age between 2 and 3 Myr). It does not show evidences of an underlying old stellar population and hosts a substantial population of WR stars.
- We have obtained direct determinations of the oxygen abundance for most of the galaxies of the group, finding very similar values in all the cases ($12+\log(\text{O}/\text{H}) = 8.0-8.2$) despite their very different absolute magnitudes. We report the first direct abundance determination for members B, E, F2, and G.
- We detect the C II $\lambda 4267$ line in the spectrum of member C. This is the first time this recombination line is reported in an H II galaxy. The C^{++}/H^+ ratio we derive from this line is too high, but this could be due to our possible overestimation of the intensity of this weak line.
- We argue that the use of traditional metallicity-luminosity relations based on the absolute B -magnitude (as those of Richer & McCall 1995, constructed for non-bursting dwarf galaxies) is not appropriate for dwarf starburst galaxies. Their luminosity is dominated by the transient contribution of the starburst to the blue luminosity, which increases dramatically the B -magnitude with respect to the pre- or post-starburst quiescent phase.
- We propose that members E and F are tidal dwarf galaxies made of gas-rich material stripped from the A+C complex because

of: (a) their high oxygen abundance (similar to that of the other galaxies of the group); (b) the absence of substantial underlying old stellar populations; (c) their kinematics.

- We propose that HCG 31 is a very complex interacting system of galaxies that is suffering several simultaneous interaction processes. A and C are the dominant members of the group and they are now merging. This merging process could be the origin of the two optical tidal tails that extend towards the northeast and southwest of the A+C complex. There was a fly-by encounter between G and the A+C complex (or one of these galaxies before the merging) and this encounter produced an H I tidal tail from the stripping of the external gas of A+C. This tail moves in or very close to the direction of the plane of the sky. Members E and F could have formed from instabilities produced in this gas-rich structure. Finally, member B is in interaction with the A+C complex. This is indicated by: (a) the strong star formation that is taking place along the tilted disk of B; (b) the presence of apparent streaming motions in the ionized gas between both objects; (c) the clear faint bridge of matter that connects B and the A+C complex.

We would like to thank José A. Caballero for providing us with a macro for NIR reduction. We thank Verónica Melo and Ismael Martínez-Delgado for permitting us to observe at CST on 2003 February 4. We are very grateful to Jorge García-Rojas for his help in the derivation of the helium abundances. We would also like to thank David Martínez-Delgado for permitting us to observe at INT on 2003 September 22 and, especially, the anonymous referee for his/her valuable comments. M.R. acknowledges support from Mexican CONACYT project J37680-E.

REFERENCES

- Allende Prieto, C., Lambert, D.L. & Asplund, M. 2001, *ApJ*, 556, 63
- Barton, E., Geller, M., Ramella, M., Marzke, R. O. & da Costa, L. N. 1996, *AJ*, 111, 40
- Benjamin, R.A., Skillman, E.D. & Smits, D.P. 2002, *ApJ*, 569, 288
- Brocklehurst M. 1971, *MNRAS* 153, 471
- Bushouse, H.A. & Stanford, S.A. 1992, *AJSS*, 79, 213
- Cairós, L.M., Vílchez, J.M., González Pérez, J.N., Iglesias-Páramo, J. & Caon, N. 2001, *AJSS*, 133, 321
- Calzetti, D. 1997, *AJ*, 113, 162
- Campos-Aguilar, A., Moles, M. & Masegosa, J. 1993, *AJ*, 106 1784
- Castellanos, M. 2000, PhD Thesis: *A comprehensive Study of High Metallicity Giant Extragalactic H II Regions*, Univ. Autónoma de Madrid
- Conti, P.S., 1991, *ApJ*, 377, 115
- Conti, P.S., Leitherer, C., & Vacca, W.M., 1996, *AJ*, 461, L87
- Davey, A.R., Storey, P.J. & Kisieliu, R. 2000, *A&ASS*, 142, 85
- Denicoló, G., Terlevich, R. & Terlevich, E. 2002, *MNRAS* 330, 69
- Dopita, M.A., Kewley, L. J., Heisler, C.A. & Sutherland, R.S. 2000, *ApJ*, 542, 224
- Duc, P.A., Brinks, E., Springel, V., Pichardo, B., Weilbacher, P. & Mirabel, I.F. 2000, *AJ*, 120, 1238
- Emelgreen, B.G., Kauffman, M. & Thomasson, M., 1993, *ApJ*, 412, 90
- Esteban, C. 2002, *RevMexAA Serie de Conferencias*, in *Ionized Gaseous Nebulae, a Conference to Celebrate the 60th Birthdays of Silvia Torres-Peimbert and Manuel Peimbert*, W. J. Henney, J. Franco, M. Martos, & M. Peña (eds), 12, 56
- Esteban, C., Peimbert, M., Torres-Peimbert, S. & Rodríguez, M. 2002, *ApJ*, 581, 241
- Fritze-von Alvensleben, U. & Gerhard O.E. 1994, *A&A*, 285, 751
- Garnett, D.R. 1992, *AJ*, 103, 1330

- Garnett, D.R., Shields, G.A., Skillman, E. D., Sagan, S. P. & Dufour, R. J. 1997, *ApJ*, 489, 63
- Garnett, D.R., Shields, G.A., Peimbert, M., Torres-Peimbert, S., Skillman, E.D., Dufour, R.J., Terlevich, E. & Terlevich, R.J. 1999, *ApJ*, 513, 168
- Garnett, D.R. 2003, in *XIII Canary Island Winter School of Astrophysics: "Cosmochemistry: The melting pot of elements"*, in press
- Guseva, N., Izotov, Y. I. & Thuan, T.X. 2000, *ApJ*, 531, 776
- Hibbard, J.E. & van Gorkom, J.H 1996, *AJ*, 111, 655
- Hibbard, J.E. & Yun, M.S. 1999, *AJ*, 118, 162
- Hibbard, J.E., van der Hulst, J.M., Barnes, J.E. & Rich, R.M. 2001, *AJ* 122, 2969
- Hickson, P., 1982, *ApJ*, 255, 382
- Hickson, P., Mendes de Oliveira, C., Huchra, J.P. & Palumbo, G.G. 1992, *ApJ*, 399, 353
- Hidalgo-Gómez, A.M. & Olofsson, K. 1998, *A&A*, 334, 45
- Hidalgo-Gómez, A.M., Sánchez-Salcedo, F.J. & Olofsson, K. 2003, *A&A*, 399, 63
- Hirashita, H. 2000, *PASJ*, 52, 107
- Holweger, H. 2001, in *AIP Conf. Ser.* 598, *Solar and Galactic Composition*, ed. R. F. Wimmer-Schweingruber (New York: Springer), 23
- Howarth I.D. & Murray J. 1990, *SERC Starlink User Note No.* 50
- Hunsberger, S.D., Charlton, J.C. & Zaritsky, D. 1996, *ApJ*, 462, 50
- Hunt, L.K., Mannucci, F., Testi, L., Migliorini, S., Stanga, R.M., Baffa, C., Lisi, F. & Vanzì, L. 1998, *AJ*, 115, 2594
- Iglesias-Páramo, J. & Vílchez, J.M. 1997, *ApJ*, 479, 190
- Iglesias-Páramo, J. & Vílchez, J.M. 1999, *ApJ*, 518, 94
- Iglesias-Páramo, J. & Vílchez, J.M. 2001, *ApJ*, 550, 211
- Izotov, Y.I. & Thuan, T.X., 1998, *ApJ*, 500, 188
- Johnson, K. E., Vacca, W.D., Leitherer, C., Conti, P. S. & Lipsy, S. J., 1999, *AJ*, 117, 1708
- Johnson, K. E. & Conti, P.S. 2000, *ApJ*, 119, 2146
- Kaler, J.B. & Lutz, J.H. 1985, *PASP*, 97, 700
- Kaufman, M., Brinks, E., Elmegreen, D.M., Thomasson, M., Elmegreen, B.G., Struck, C. & Klaric, M. 1997, *AJ*, 114, 2323
- Kauffman, G. & White, S.D.M. 1993, *MNRAS*, 261, 921
- Kennicutt, R.C. 1998, *ApJ*, 498, 541
- Kingdon, J. & Ferland, G.J. 1995, *ApJ*, 442, 714
- Kunth, D. & Schild, H. 1986, *A&A*, 169, 71
- Landolt A.U. 1992, *AJ*, 104, 340
- Leitherer, C. & Heckman, T.M. 1995, *ApJS*, 96, 9
- Leitherer, C., Schaerer, D., Goldader, J.D., González-Delgado, R.M., Robert, C., Kune, D.F., de Mello, D.F., Devost, D. & Heckman, T.M. 1999, *ApJS*, 123, 3 (*STARBURST 99*)
- Massey P., Strobel K., Barnes J.V. & Anderson E. 1988, *ApJ* 328, 315
- Mazzarella, J.M. & Boroson, T.A. 1993, *ApJS*, 85, 27
- McGaugh, S.S. 1994, *ApJ*, 426, 135
- Mendez de Oliveira, C. & Hickson, P. 1994, *ApJ*, 427, 684
- Méndez, D.I. & Esteban, C. 1999, *AJ* 118, 2733
- Méndez, D.I., Cairós, L.M., Esteban, C. & Vílchez, J.M. 1999, *AJ* 117, 1688
- Moles M., del Olmo, A., Perea, J., Masegosa, J., Márquez, I. & Costa, V. 1994, *A&A*, 285, 404
- Moshir, M. et al. 1990, in *The IRAS Faint Source Catalog, Version 2.0*, Pasadena:IPAC
- Noeske, K.G., Papaderos, P., Cairós, L.M. & Fricke, K.J. 2003, *A&A*, 410, 481

- Noguchi, M. & Ishibashi, S. 1986, MNRAS, 219, 305
- Noguchi, M. 1988, A&A, 203, 259
- O'Halloran, B., Metcalfe, L., McBreen, B., Laureijs, R., Leech, K., Delaney, M., Watson, D. & Hanlon, L. 2002, 575, 747
- Olofsson, K. 1995, A&ASS, 111, 57
- Peimbert, A. 2003, ApJ, 584, 735
- Peimbert M. & Costero, R. 1969, Bol. Obs. Tonantzintla y Tacubaya, 5, 3
- Peña, M. & Ayala, S. 1993, RevMexAA, 27, 171
- Pilyugin, L.S. 2001a, A&A, 369, 594
- Pilyugin, L.S. 2001b, A&A, 374, 412
- Plana, H., Amram P. & Mendez de Oliveira, C. 2002, in *Galaxies: the third dimension*, ASP conference Series, Vol 282, p. 238, M. Rosado, L. Binette and L. Arias (eds.)
- Quinet, P. 1996, A&AS, 116, 573
- Richer, M.G. & McCall, M.L. 1995, ApJ, 445, 642
- Richer, M.G., Georgiev, L., Rosado, M., Bullesjos, A., Valdez-Gutiérrez, M. & Dultzin-Hacyan, D. 2003, A&A, 397, 99
- Rieke, G.H. & Lebofsky, M.J. 1985, ApJ, 288, 618
- Rodríguez, M. 2003, ApJ, 590, 296
- Rodríguez, M. & Rubin, R.H. 2003, in *Recycling Intergalactic and Interstellar Matter*, IAU Symposium Series, Vol. 217 eds. P.-A. Duc, J. Braine, & E. Brinks, in press (astro-ph/0312246)
- Rubin, V.C., Hunter, D.A., & Ford, W.K., Jr., 1990, ApJ, 365, 86
- Sanders, D.B., Soifer, B.T., Elias, J.H., Madore, B.F., Matthews, K., Neugebauer, G. & Scoville, N.Z. 1988, ApJ, 325, 74
- Sargent, W.L.W. & Searle, L. 1970, ApJ, 162, L155
- Schaerer, D. & Vacca, W.C. 1998, ApJ, 497, 618
- Schlegel, D.J., Finkbeiner, D.P. & Davis, M. 1998, ApJ, 500, 525
- Schweizer, F. 1982, ApJ, 252, 455
- Shaw, R.A. & Dufour, R.J. 1995, PASP, 107, 896
- Skillman, E.D., Kennicutt, R.C. & Hodge, P.W. 1989, ApJ, 347, 875
- Smith, L.F., Shara, M.M. & Moffat, A.F.J. 1996, MNRAS, 281, 163
- Stasińska, G. 1990, A&AS, 83, 501
- Stasińska, G. & Leitherer, C. 1996, ApJS, 107, 661
- Sulentic, J. W., Rosado, M., Dultzin-Hacyan, D., Verdes-Montenegro, L., Trinchieri, G., Xu, C. & Pietsch, W. 2001, AJ, 122, 2993
- Taylor, C. L., Brinks, E. & Skillman, E. D., 1993, AJ, 105, 128
- Taylor, C., Brinks, E., Grashuis, R. M. & Skillman, E. D., 1995, ApJS, 99, 427
- Taylor, C., Thomas, D., Brinks, E., & Skillman, E. D., 1996, ApJS, 107, 143
- Telles, E. & Terlevich, R.J. 1995, MNRAS 275, 1
- Thuan, T.X. 1991, in *Massive stars in starbursts*, C. Leitherer, N.R. Walborn, T.M. Heckman & C.A. Norman (eds), Cambridge University Press, Cambridge, p.183
- Vacca, W.D. & Conti, P.S., 1992, ApJ, 401, 543
- van der Hulst, J.M. 1979, A&A, 75, 97
- Vanzi, L., Hunt, L.K., Thuan, T.X. & Izotov, Y.I. 2000, A&A, 363, 493
- Vanzi, L., Hunt, L.K. & Thuan, T.X. 2002, A&A, 390, 481
- Veilleux, S. & Osterbrock, D.E. 1987, ApJS, 63, 295
- Verdes-Montenegro, L., del Olmo, A., Perea, J., Athanassoula, E., Márquez, I. & Augarde, R. 1997, A&A, 321, 409
- Verdes-Montenegro, L., Yun, M.S., Perea, J., del Olmo, A. & Ho, P.T.P. 1998, ApJ, 497, 89
- Verdes-Montenegro, L., Yun, M.S., Williams, B.A., Huchtmeier, W.K., del Olmo, A. & Perea, J. 2001, A&A, 377, 812

- Verdes-Montenegro, L., del Olmo, A., Iglesias-Páramo, J. I., Perea, J., Vílchez, J.M., Yun, M.S. & Huchtmeier, W.K. 2002, A&A, 396, 815
- Verner, E.M., Verner, D.A., Baldwin, J.A., Ferland, G.J. & Martin, P.G. 2000, ApJ, 543, 831
- Vílchez, J.M & Iglesias-Páramo, J. 1998, ApJ, 508, 248
- Weilbacher, P.M. & Duc, P.A. 2001, in *Dwarf Galaxies and their Environments*, K. de Boer, R.J. Dettmar & U. Klein (eds.), 269
- Weilbacher, P.M., Duc, P.A. & Fritze-von Alvensleben, U. 2003, A&A, 397, 545
- Whitford, A.E. 1958, AJ, 63, 201
- Williams, B.A., McMahon, P.M. & van Gorkom, J.H. 1991, AJ, 101, 1957
- Yun, M.S., Ho, P.T.P. & Lo, K.Y. 1994, Nature, 372, 530
- Yun, M.S., Verdes-Montenegro, L., del Olmo, A. & Perea, J. 1997, ApJ, 475, L21
- Zhang, H. L. 1996, A&AS, 119, 523

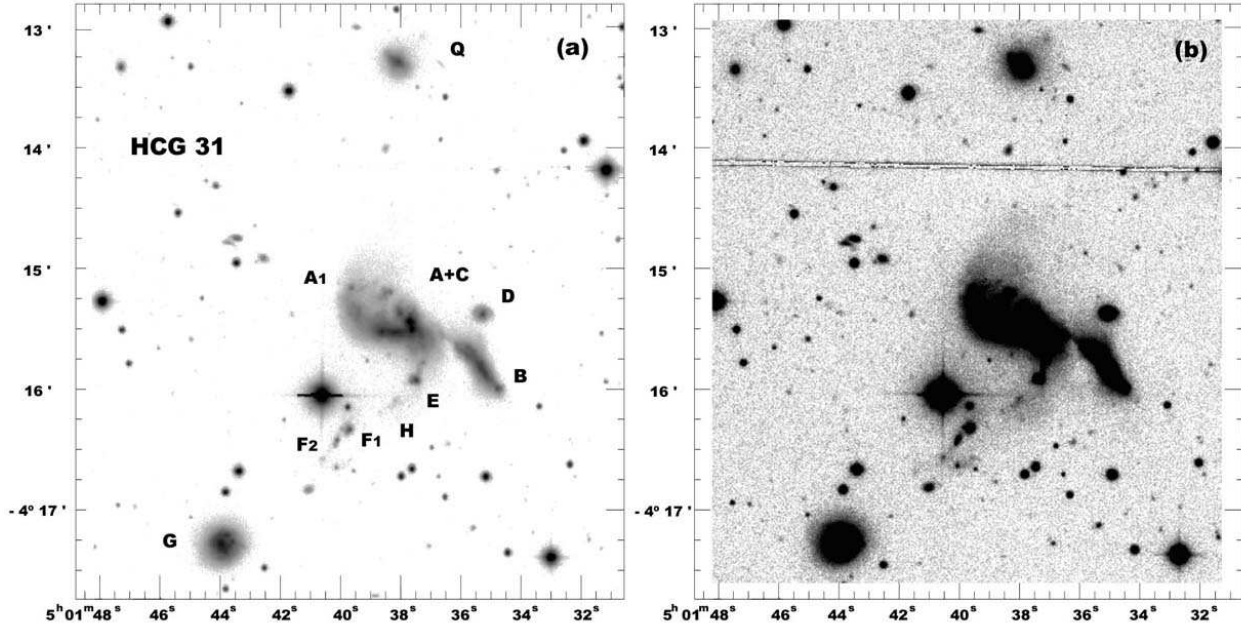


Fig. 1.— Deep optical image of HCG 31 in the R filter. All the individual galaxies of the group, as well as knot A1 (see text), are indicated and labeled. Image (b) is a saturated version of (a) showing the faintest structures.

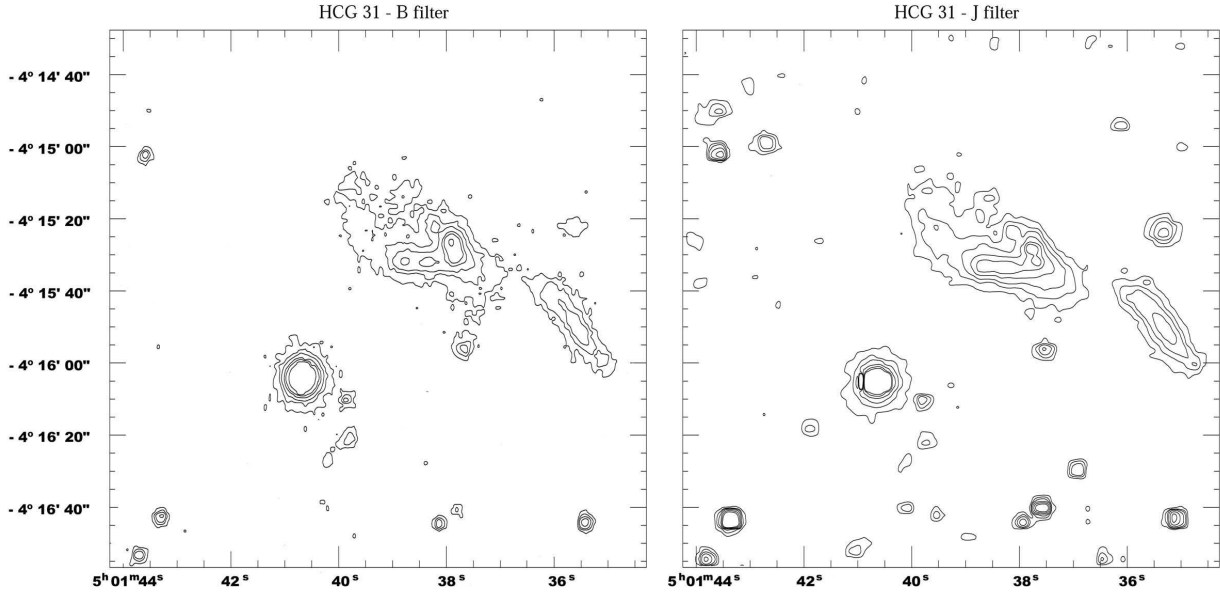


Fig. 2.— Logarithmic contour maps of the central part of HCG 31 in B and J filters. The external contour corresponds to the 3σ level in both maps.

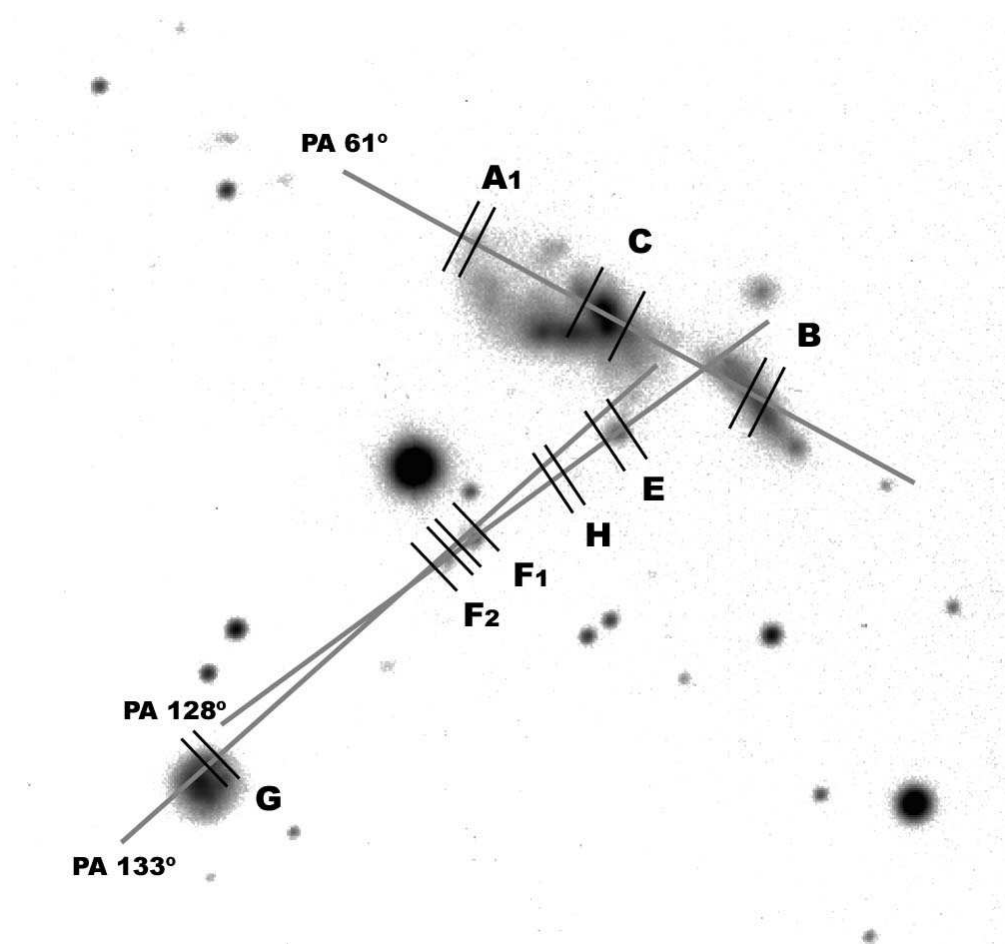


Fig. 3.— Slit positions over V image. The spatial extension of the different zones from which we have extracted the one-dimensional spectra are indicated with ticks.

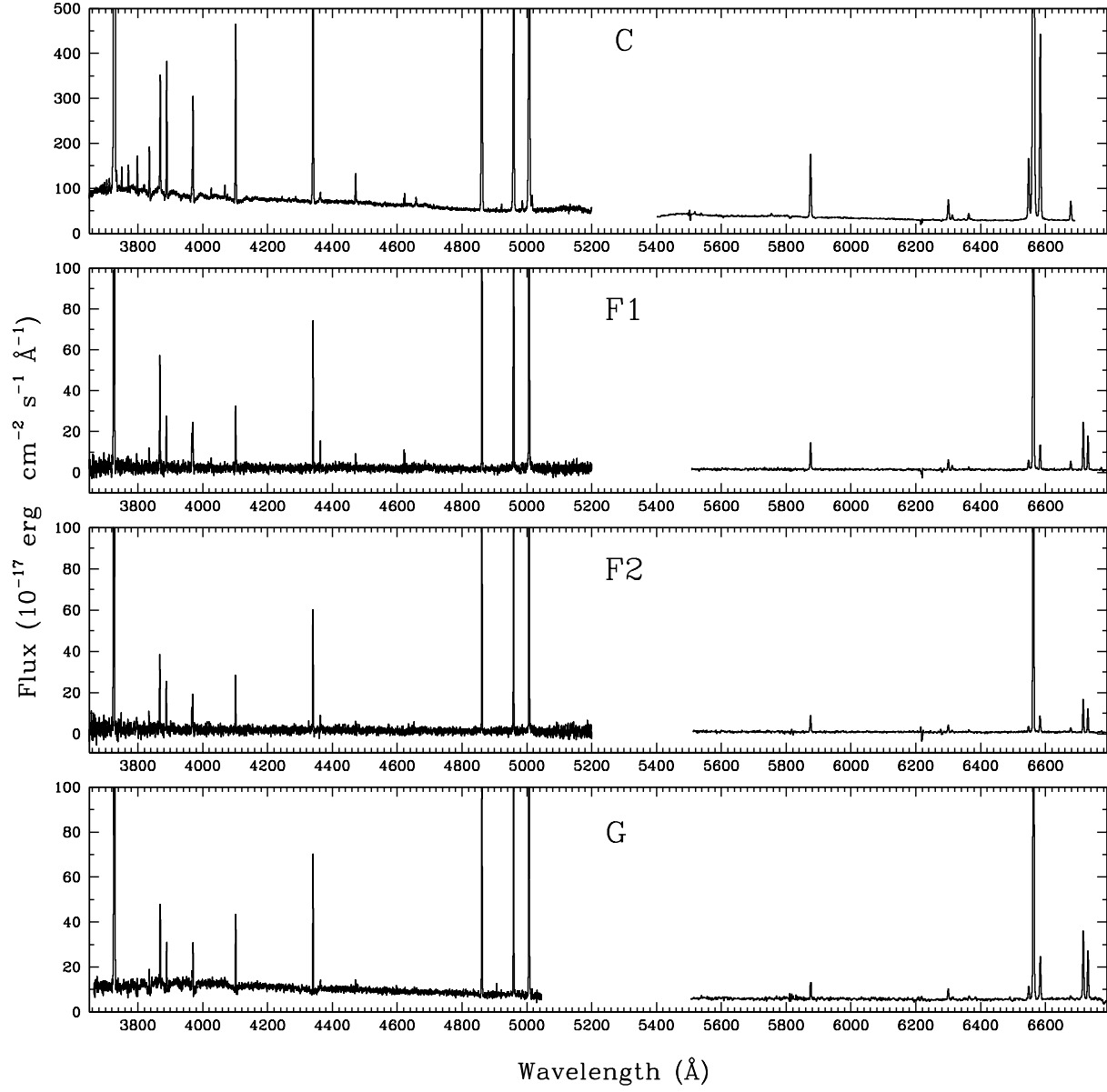


Fig. 4.— ISIS WHT spectra of members C, F1, F2 and G. The spectra have been scaled down in flux in order to distinguish the faint lines.

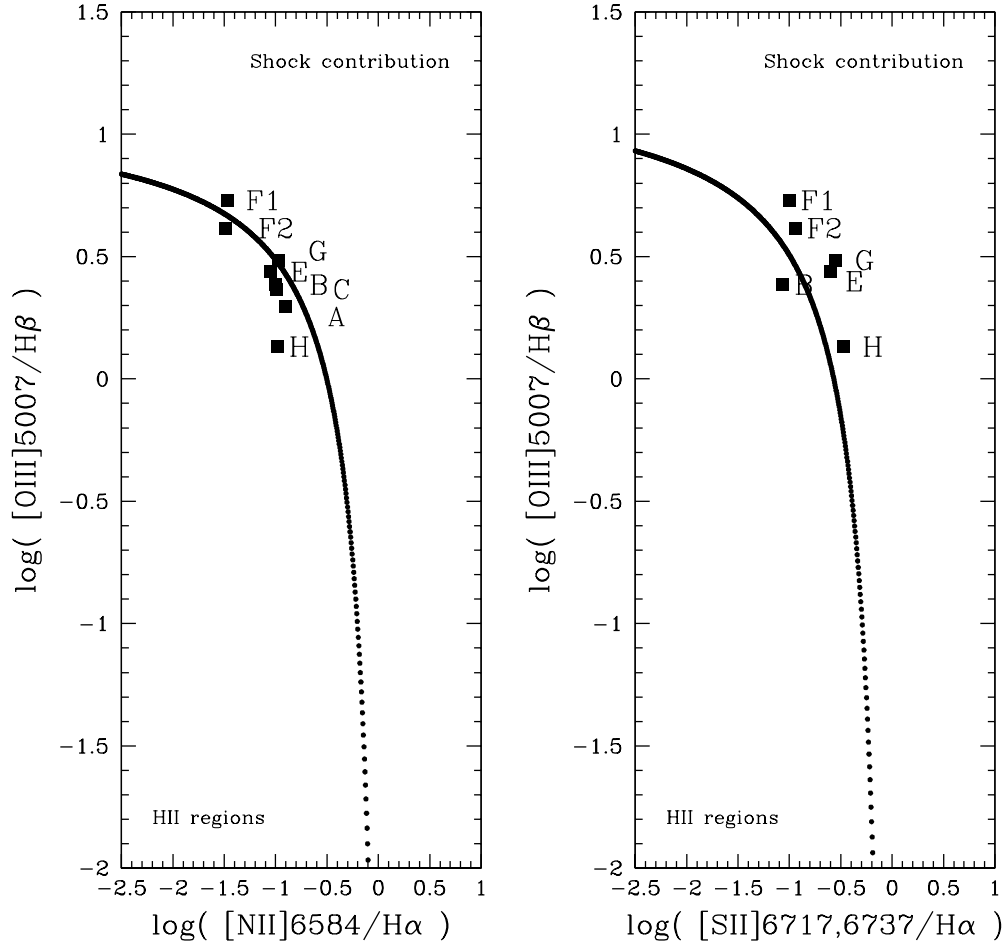


Fig. 5.— Physical properties of the emission line regions in HCG 31. The flux line ratios are indicated. The solid lines give the limit for ionization by a zero age starburst, following Dopita et al. (2000).

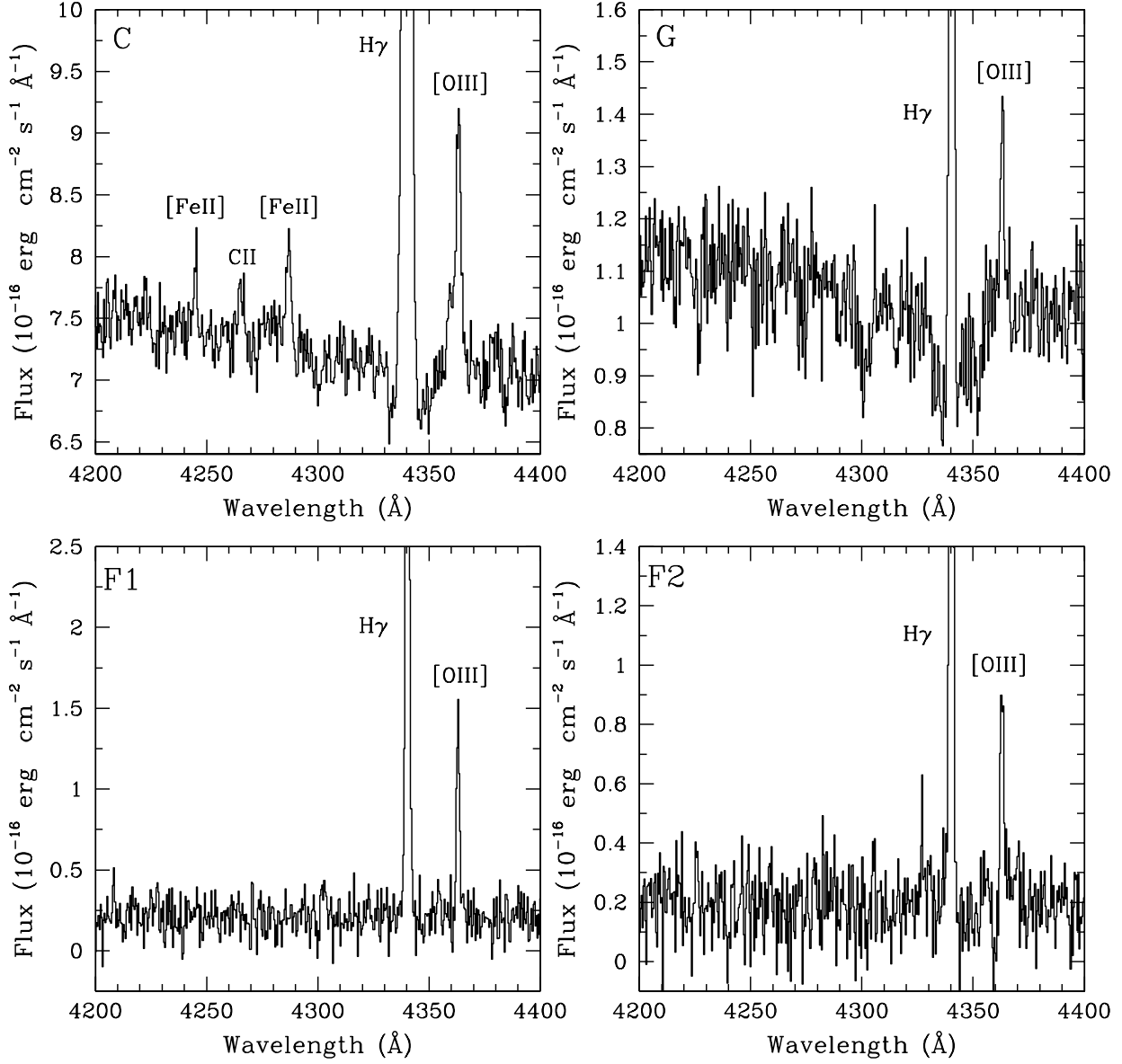


Fig. 6.— Detail of the spectra of members C, F1, F2, and G showing the zones around the [O III] $\lambda 4363$ emission line. Member C also shows the C II $\lambda 4267$ and [Fe II] $\lambda\lambda 4244, 4287$ emission lines. H γ shows a weak absorption due to the underlying stellar population in members C and G.

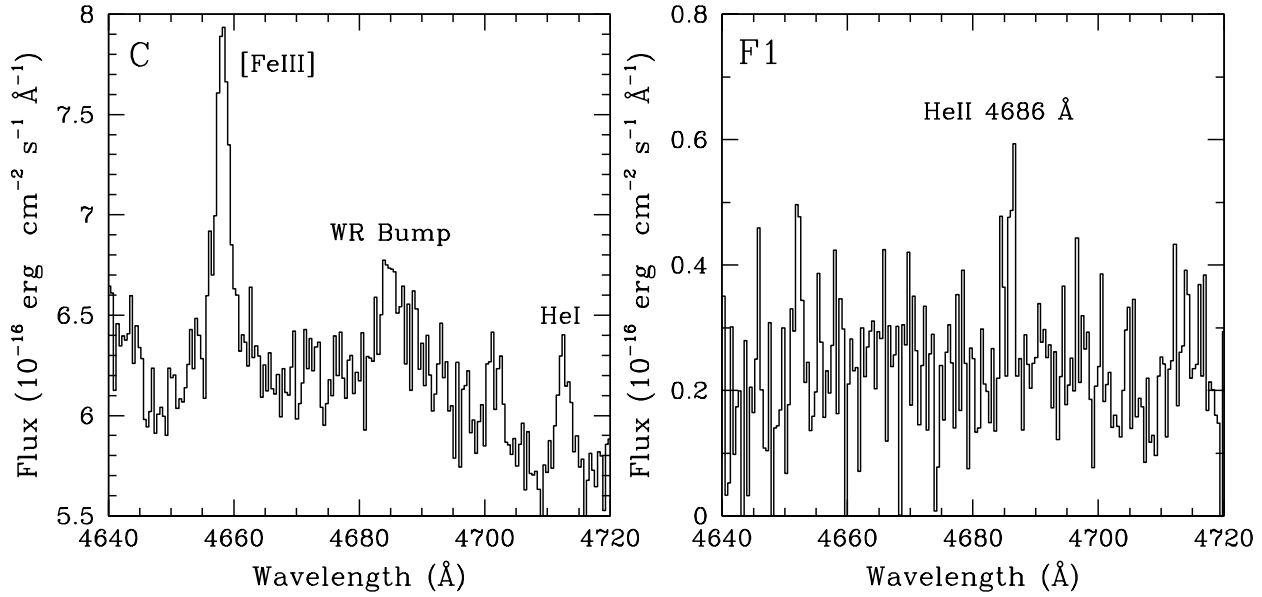


Fig. 7.— Detail of the spectra of members C and F1 showing the WR bump or the He II $\lambda 4686$ emission. [Fe III] $\lambda 4658$ and He I $\lambda 4713$ emission lines are also clearly observed in C.

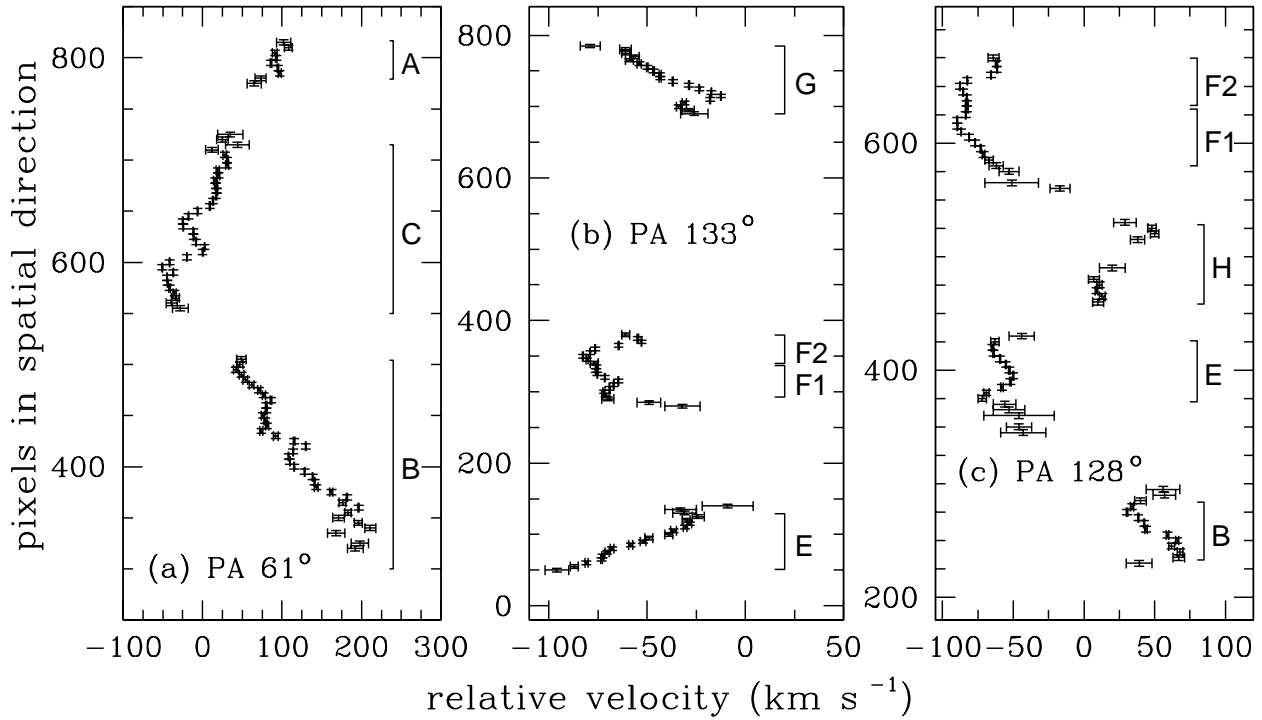


Fig. 8.— a, b and c: Position-velocity diagrams for the three slit position observed in HCG 31 analyzed in $1''$ bins. The horizontal bars represent the uncertainty of the Gaussian fitting for each point. The location and extension of the different galaxy members is also indicated. North is up in (a) and southeast is up in (b) and (c).

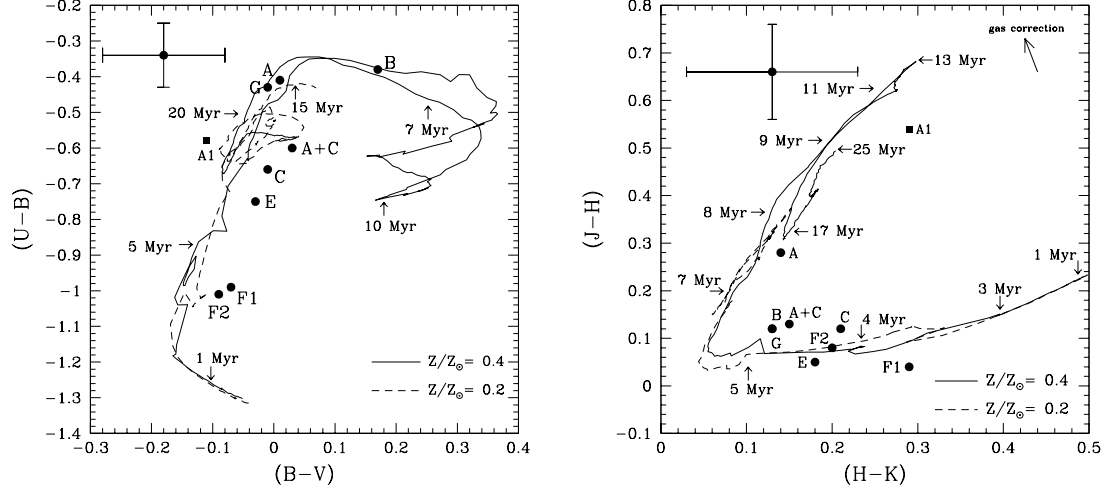


Fig. 9.— (a) $(U - B)$ versus $(B - V)$ and (b) $(H - K_S)$ versus $(J - H)$ values of the objects and STARBURST 99 (Leitherer et al. 1999) predictions for an instantaneous burst with a Salpeter IMF. We have marked with arrows some ages of the $Z/Z_\odot=0.4$ model, showing the temporal evolution of the burst. The error bars indicate the average uncertainties in the data. We have included the photometric values derived for A1 with a square.

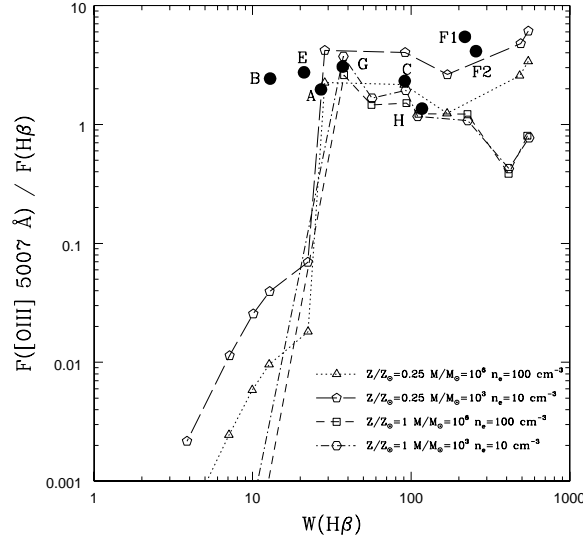


Fig. 10.— $F([\text{O III}] \lambda 5007) / F(\text{H}\beta)$ versus $W(\text{H}\beta)$. Models by Stasińska & Leitherer (1996). Tracks correspond to sequences of different metallicities and electronic densities. Each symbol marks the position of the models at 1 Myr interval, starting in the upper-right corner of the diagram with an age of 1 Myr. F1 and F2 are located between the 2 and 3 Myr symbols.

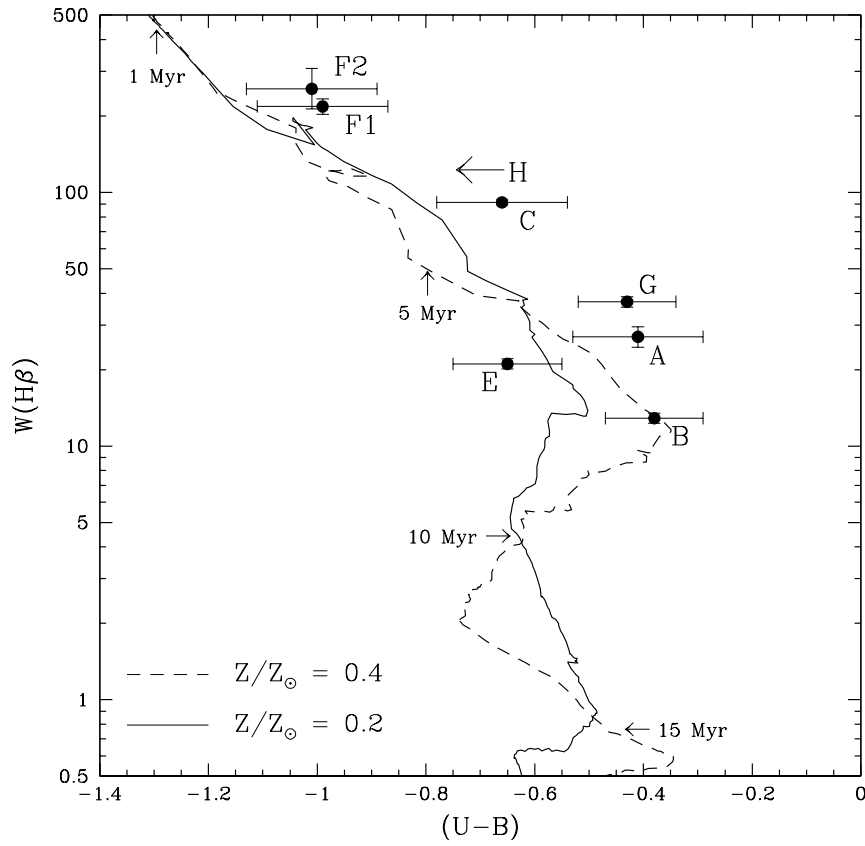


Fig. 11.— $W(\text{H}\beta)$ versus $(U - B)$ for members in HCG 31 and STARBURST 99 (Leitherer et al. 1999) predictions for an instantaneous burst with a Salpeter IMF. We have marked with arrows some ages of the $Z/Z_{\odot}=0.4$ model, showing the temporal evolution of the burst.

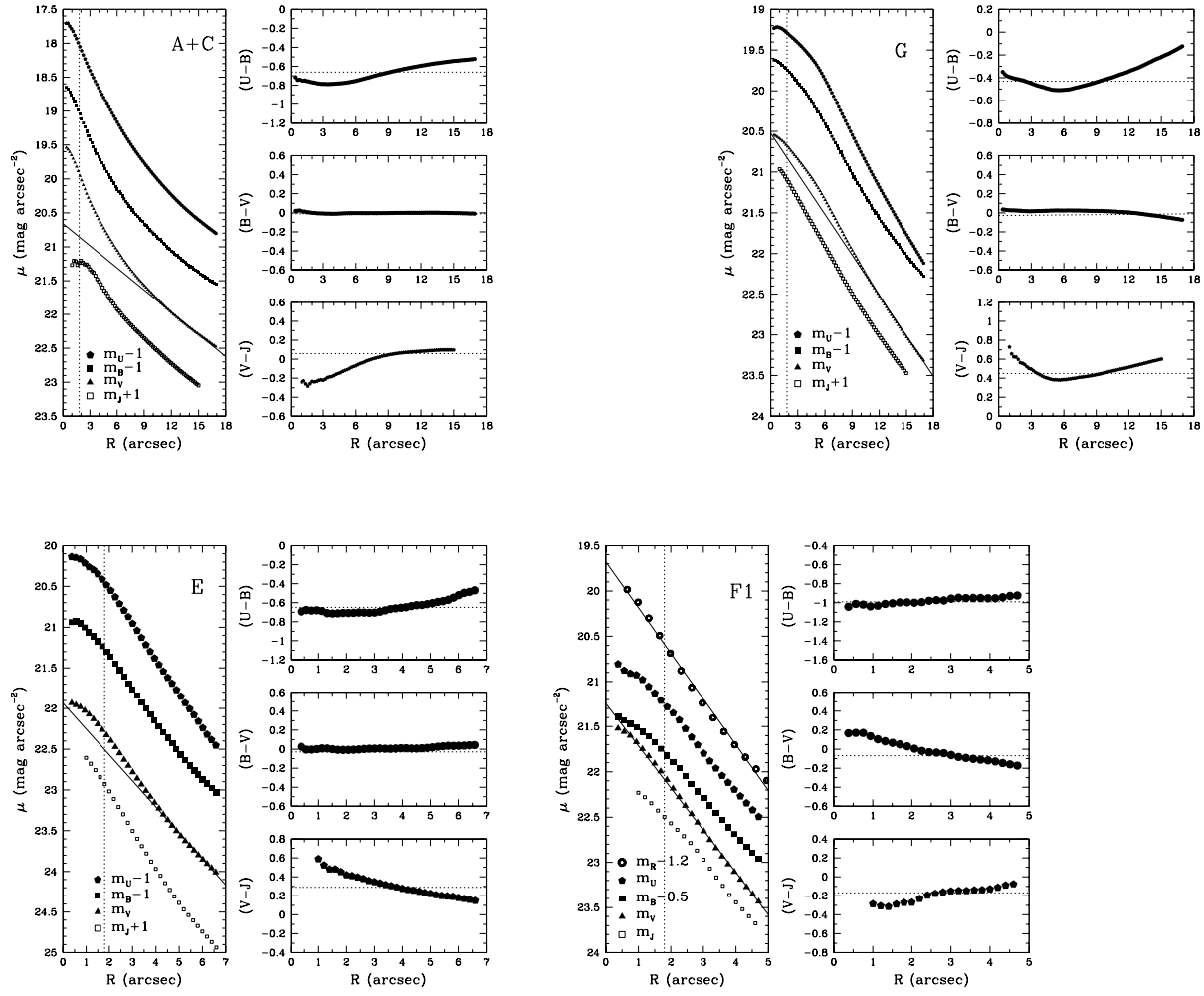


Fig. 12.— Surface brightness and color profiles for the A+C complex and members G, E, and F1 of HCG 31. The line in the surface brightness diagrams is an exponential law fitting to the V profile, whereas the dotted vertical line is the average seeing. The dotted horizontal line in the color profile diagrams indicates the average color derived for each system. For F1 we also show the R surface brightness profile and an exponential law fitting to it.

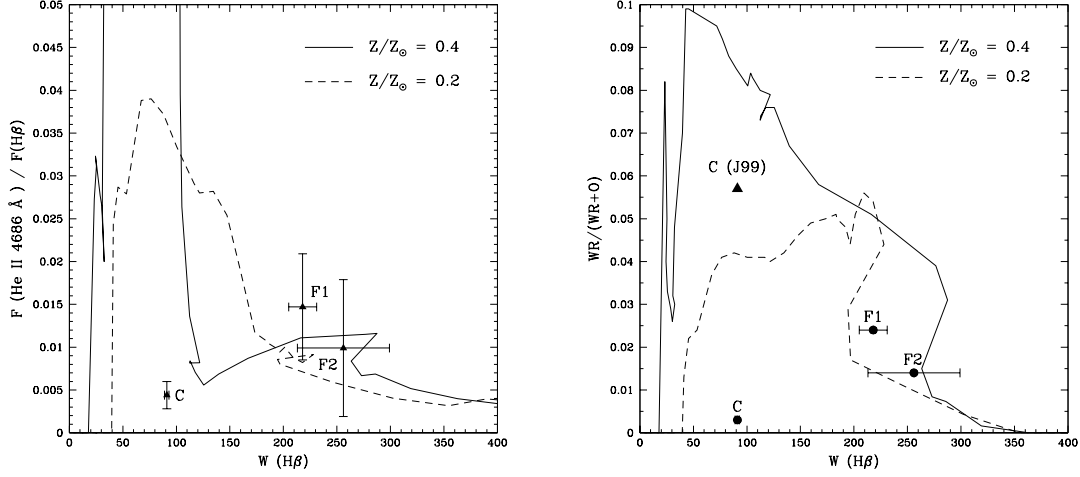


Fig. 13.— (a) $F(\text{He II})$ versus $W(\text{H}\beta)$ for Schaerer & Vacca (1998) starbursts models compared with our results for C, F1, and F2. (b) $WR/(WR+O)$ versus $W(\text{H}\beta)$ for Schaerer & Vacca (1998) models. We include our results from optical spectroscopy (*circles*) and the one obtained from the He II $\lambda 1640$ emission line flux (*triangle*) by Johnson et al. (1999) using Schaerer & Vacca (1998) calibration (their eq. 18).

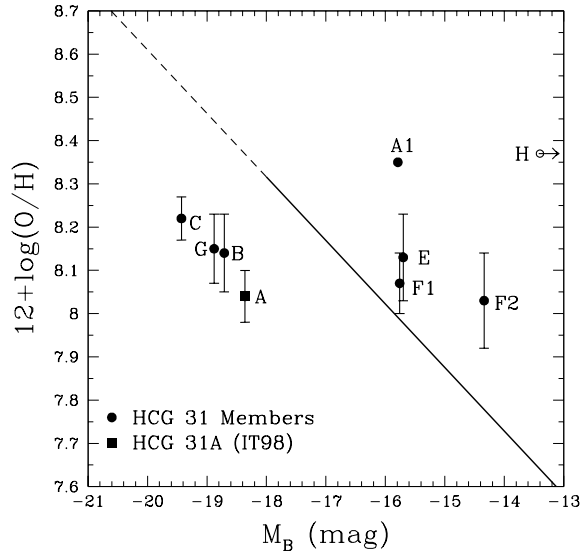


Fig. 14.— The relation between luminosity and metallicity for the galaxies in HCG 31. The solid line is the relation for dwarf irregulars found by Richer & McCall (1995), while the dashed line is an extrapolation of it. The O/H ratios for A1 and H are estimations based on empirical calibrations. The O/H ratio for member A is from Izotov & Thuan (1998) (IT98).

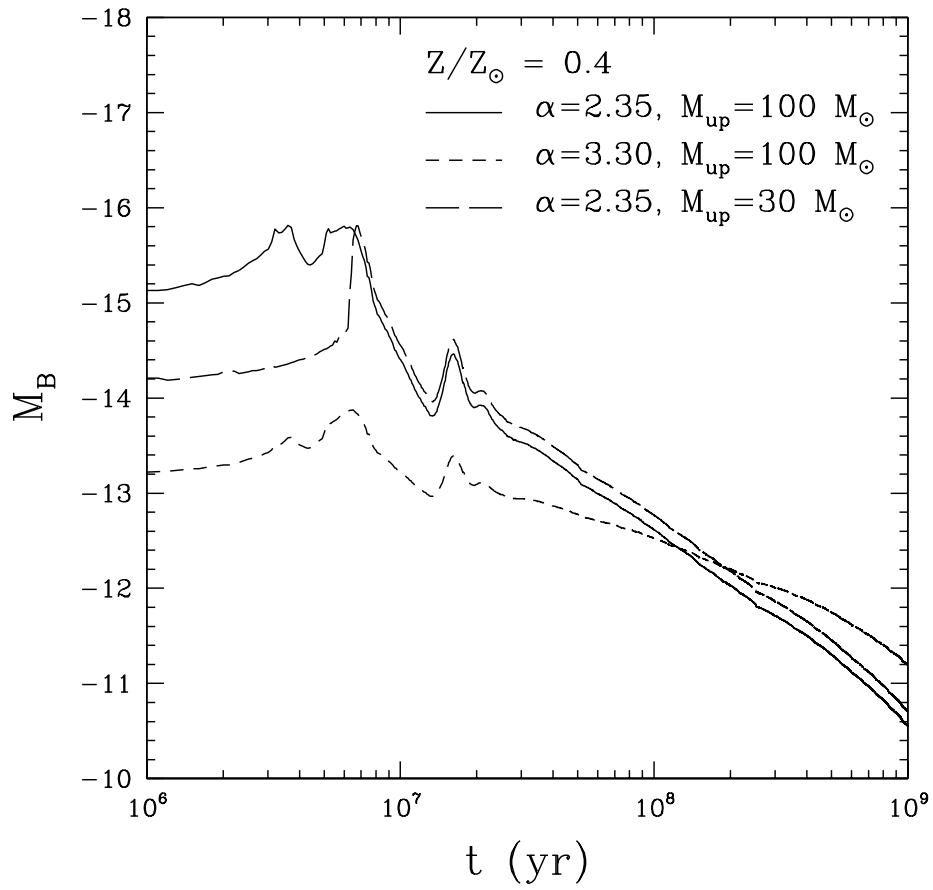


Fig. 15.— M_B evolution versus time for the indicated STARBURST 99 (Leitherer et al. 1999) models.